Diagnoses of an Axisymmetric Model of Tornadogenesis

Robert Peter Davies-Jones [a]

[a] *Remote corner of a black hole*

D-J Research Papers, **3**.

June 2025

Corresponding author: Dr. Robert Davies-Jones, bobdj1066@yahoo.com

ABSTRACT

A simulation of axisymmetric tornadogenesis is examined in greater detail than was possible 17 years ago. The results are reanalyzed using three approaches. First, the evolutions of 30 fields are visualized using animations of plots with fixed contours. Second, various properties of a parcel that enters the tornado are graphed versus time. Third, accurate budgets are produced for mean angular momentum, helicity, and kinetic energy in a surface-based cylindrical control volume that surrounds the eventual tornado. These means depend on various fluxes through the cylinder's surfaces.

The model is initially in a helical state that resembles a slowly decaying midlevel mesocyclone. This balanced flow is upset by the drag exerted by rain. Sudden tremendous changes occur just prior to tornadogenesis as angular momentum is advected downward and inward into the cylinder. Cylinder means of helicity and Lamb-vector magnitude start increasing rapidly just minutes prior to tornado formation. The former is much larger than the latter so the tornadic vorticity is very streamwise. Huge increase in convergence on the tornado scale explains the rapidity of tornado formation.

The parcel that reaches the tornado passes underneath the rainy downdraft just before outflow from this downdraft could block it. Loss of angular momentum to the ground enables the parcel to almost reach the axis and spin rapidly. At tornado entry, its helicity has increased a hundred times. Its helicity gain is due to the integral over time of the scalar product of its vorticity with its gradient of kinetic energy minus static energy.

SIGNIFICANCE STATEMENT

There is still no widely accepted theory of how tornadoes form despite 75 years of observational programs, 50 years of 3D supercell modelling, and recent excellent visualizations of results. The approach used here is to seek understanding of tornado formation in a toy model that still replicates features of real-life tornadogenesis. The toy model simplifies the problem by assuming that the flow is axisymmetric with constant density and eddy viscosity. The evolutions of many variables are easily visualized using animations of contour plots. Model diagnostics show how parcels with modest angular momentum are brought along the ground to near the axis to form a tornado and how these parcels suddenly acquire their tremendous helicity, kinetic energy, and pressure deficit.

1. Introduction

This paper extensively diagnoses the results of an axisymmetric model of tornadogenesis (Davies-Jones 2008; hereafter DJ08). Of particular interest are the acquisition of huge density (scalar product of velocity and vorticity) by parcels that enter the tornado and the role played by the Lamb vector (vector product of velocity and vorticity) in tornadogenesis. A Beltrami flow is one without a Lamb vector. Even though it is helical, it is incapable of evolving so at least a small Lamb vector is somehow vital for tornado formation for reasons discovered herein. Davies-Jones (2025a; hereafter DJ25), developed theory that describes how parcels flow can acquire tremendous helicity density (hereafter abbreviated to helicity). A related paper (Davies-Jones 2025b) uses an analytical model (Davies-Jones 2000) to illustrate the basic physical processes involving changes in parcel helicity. This model is of limited interest to tornado researchers because the primary flow in the analytical model does not resemble a supercell and is unable to generate large amplifications of helicity. A third paper (Davies-Jones 2025c) reveals how the circulation of a tornado's parent updraft needs a small amount of cyclonic vorticity at the updraft edge in order to grow.

The DJ08 model demonstrates that a tornado can form in a flow that is axisymmetric and without any mechanism for tilting horizontal baroclinic vorticity into the vertical. Rotunno and Bluestein (2024) stated that "it provides ... the closest mathematical connections between the dynamics of supercells and tornadoes characterized by the endwall vortex". It is used here to demonstrate how large helicities can arise in simulated tornadoes and to perform diagnoses that have been made possible by advances in computing. The closed domain is large enough to include a complete storm-scale circulation that spawns and interacts with the vortex. The flow is unstratified to avoid buoyancy oscillations. The grid is unstaggered so all variables are defined at the boundaries. Variables are nondimensionalized using the height H of the domain as the length scale, the amplitude W_0 of the initial vertical wind as the velocity scale, and H/W_0 as the time scale. The radius of the cylindrical domain is $R = 0.7042H$.

The initial condition (at time zero) is a balanced Beltrami flow with an abnormality of $6.283/H$. It describes an updraft of radius $0.442H$ that is rotating cyclonically at midlevels around a low-pressure center surrounded by a concentric downdraft that revolves cyclonically but has anticyclonic vertical vorticity (see Fig. 1and animations A, B, C at $t = 0$). There is

very little angular momentum (AM) near the ground. This flow crudely resembles a midlevel mesocyclone or a low-precipitation supercell (Davies-Jones et al. 1976) if we assume $H = 12$ km and $W_0 = 33.3$ m s^{-1}. The model equations are nondimensionalized using H as the unit of length and $H/W_0 = 360$ sec as the unit of time. In this paper, values listed without units are nondimensional.

The boundary conditions are no slip on the tangential wind and free slip on the radial or vertical wind to accommodate the initial condition and to allow strong interaction of a vortex with the ground. These conditions allow the intense inflow and inward vorticity that develop at the ground in real tornadoes (Davies-Jones et al. 1978).

The eddy viscosity in supercell models is not fixed; it is dependent on the square root of turbulent kinetic energy, which is computed via a complicated prognostic equation. The turbulence parameterization does not include the effects of helicity on turbulence (Lilly 1986) and its applicability to the boundary layer, corner region, and core of a tornado is debatable (Wang et al. 2020). For simplicity and ease of interpretation, the eddy viscosity is assumed unrealistically to be constant in the DJ08 model.

If the initial Beltrami state is unperturbed, the flow remains Beltrami by slowly decaying without changing shape. At nondimensional time $t = 6$, the amplitudes of linear quantities apart from pressure have diminished by 11% and those of quadratic quantities and pressure have declined by 21%.

The model is unbalanced by loading the flow with a prescribed release of hydrometeors through the top above the updraft. This process creates a rain curtain that descends near the updraft–downdraft interface. The associated rain-induced downdraft and its outflow radically alters the streamines, causing the corner flow of the mesocyclone to collapse and a tornado to form through transport of AM downward and inward toward the axis.

The fall speed of the hydrometeors is $W_0/4$ or 8.3 m s^{-1}, which is roughly that of large rain drops. In a calm atmosphere, it would take four units of time after release for a rain drop to reach the ground. For future reference, we define a mesocyclone as a cyclonic vortex with core radius greater than 2 km ($H/6$), a quasi-tornado (QT) as a vortex with core radius less than 2 km that does not break the thermodynamic speed limit (Fiedler 1994), and a tornado as a vortex that does break the speed limit. The thermodynamic speed limit here is assumed to 33.3 m s^{-1}, the initial maximum updraft speed. Only a QT occurs in the model when the ground boundary conditions are changed to no-stress.

Although the flow is unrealistically simple, nevertheless it replicates several observed features of tornadogenesis. The model reproduces on the mesocyclone scale an anticyclonic clear-slot intrusion of descending air and a collapsing top. On the small scale, it generates a cyclonic tornado with winds that easily exceed the speed limit by concentrating barotropic vorticity. The updraft becomes very narrow near the ground and is surrounded by downdraft with mostly anticyclonic vorticity. The tornado has an axial jet capped by a vortex breakdown that is an abrupt transition to a QT aloft. In the terminology adopted herein, the axial jet is a genuine tornado while the vortex above the breakdown is labelled a QT. Maximum winds in the QT are roughly at the speed limit. The tornado forms at $t = 5.4$. The tornadic windspeed reaches maximum intensity at $t = 6.1$. The flow becomes more unrealistic after this time as a pressure-driven axial downdraft penetrates almost to the surface and replaces the axial updraft. The tornado is filled from above and decays at $t = 6.9$.

DJ08 conducted an experiment in which buoyant bubbles were released beneath the updraft instead of hydrometeors above it. No vortex formed because the drag force displaced angular momentum upward instead of downward.

Three different approaches are used here to show how tornadogenesis proceeds in the model. First, we examine animations that depict the evolution of helicity, AM, kinetic energy (KE), and other fields. Secondly, we find how quantities such as helicity and AM vary along the trajectory of a parcel that enters the tornado. Potential difficulties associated with a parcel descending into a ground-based layer where the velocity is undefined (Vande Guchte and Dahl 2018) are absent since the grid is unstaggered. Lastly, we set up a cylindrical control volume around the eventual tornado and show how the volume average of helicity, AM, and KE depend on fluxes into this volume.

2. Derived equations

This section obtains the equations that we use to diagnose the results of the DJ08 model The flow is axisymmetric, incompressible, unstratified, and viscous with constant kinematic eddy viscosity ν_e. The equations governing motion and mass conservation are

$$\frac{D\mathbf{v}}{Dt} \equiv \frac{\partial \mathbf{v}}{\partial t} + \nabla \frac{q^2}{2} - \mathbf{v} \times \boldsymbol{\omega} = -\nabla\sigma - g q_L \mathbf{k} + \mathbf{F}, \tag{2.1}$$

$$\nabla \cdot \mathbf{v} = 0, \tag{2.2}$$

Here, t is time, $D/Dt \equiv \partial/\partial t + \mathbf{v}\bullet\nabla$ is the material derivative, $\mathbf{v}$ is the wind vector, $q \equiv |\mathbf{v}|$ is the windspeed, $\boldsymbol{\omega} \equiv \nabla\times\mathbf{v}$ is the vorticity vector, $\mathbf{v}\times\boldsymbol{\omega}$ is the Lamb vector, $\sigma \equiv c_pT + gz$ is the static energy (the sum of enthalpy and potential energy), g is the acceleration due to gravity, z is height, q_L is the rain mixing ratio, $\mathbf{k}$ is the unit upward vector, $-gq_L\mathbf{k}$ is the hydrometeor drag, and $\mathbf{F} = -\nu_e\nabla\times\boldsymbol{\omega}$ is the viscous force. The Reynolds number, W_0H/ν_e, is 2000. In (2.1), the gradient of static energy is equivalent to the nonhydrostatic pressure-gradient force per unit mass. In cylindrical coordinates (r, ϕ, z), let $\mathbf{v} \equiv (u, v, w)$ and $\boldsymbol{\omega} \equiv (\xi, \eta, \zeta)$ where $\eta \equiv \partial u/\partial z - \partial w/\partial r$. We define a streamfunction ψ such that

$$u \equiv -\frac{1}{r}\frac{\partial\psi}{\partial z}, w \equiv \frac{1}{r}\frac{\partial\psi}{\partial r}. \tag{2.3}$$

In terms of ψ and the angular momentum $M \equiv vr$,

$$(\xi, \eta, \zeta) = \left(-\frac{1}{r}\frac{\partial M}{\partial z}, -\frac{1}{r}\frac{\partial^2\psi}{\partial z^2} - \frac{1}{r}\frac{\partial^2\psi}{\partial r^2} + \frac{1}{r^2}\frac{\partial\psi}{\partial r}, \frac{1}{r}\frac{\partial M}{\partial r}\right). \tag{2.4}$$

The DJ08 model uses a streamfunction-vorticity formulation. It solves prognostic equations for v, η, and q_L, and a diagnostic equation for ψ [i.e., the azimuthal component of (2.4)]. In this paper, we solve for static energy at each time step for accurate computation of diagnostic quantities.

We now derive the governing equations for AM, KE, and helicity. Multiplying the azimuthal equation of motion by r yields the angular-momentum equation,

$$\frac{DM}{Dt} = \nu_e\left(\nabla^2 M - \frac{2}{r}\frac{\partial M}{\partial r}\right). \tag{2.5}$$

By (2.4), the advection of AM, $-\mathbf{v}\bullet\nabla M$, is equal to the azimuthal component of the Lamb vector**.** From $\mathbf{v}\bullet$(2.1), the equation governing parcel KE is

$$\frac{D}{Dt}\frac{q^2}{2} = -\mathbf{v}\cdot\nabla\sigma - gq_Lw + \mathbf{v}\cdot\mathbf{F}. \tag{2.6}$$

[The color coding of terms in some equations correspond to colored curves in later figures.] Equivalently,

$$\frac{\partial}{\partial t}\frac{q^2}{2} = -\mathbf{v}\cdot\nabla B - gq_Lw + \mathbf{v}\cdot\mathbf{F} \tag{2.7}$$

where the Bernoulli function B is defined by

$$B \equiv \frac{q^2}{2} + \sigma. \tag{2.8}$$

Deriving the governing equation for helicity, $h \equiv \mathbf{v} \bullet \boldsymbol{\omega}$, is more complicated. Taking the curl of (2.1) and utilizing (2.2) provides the vorticity equation

$$\frac{D\boldsymbol{\omega}}{Dt} = (\boldsymbol{\omega} \cdot \nabla)\mathbf{v} - g\nabla q_L \times \mathbf{k} + \nabla \times \mathbf{F}. \tag{2.9}$$

By the product rule for derivatives,

$$\frac{Dh}{Dt} \equiv \frac{D}{Dt}(\boldsymbol{\omega} \cdot \mathbf{v}) = \boldsymbol{\omega} \cdot \frac{D\mathbf{v}}{Dt} + \mathbf{v} \cdot \frac{D\boldsymbol{\omega}}{Dt}. \tag{2.10}$$

Introducing (2.9) and (2.1) into (2.10) produces the helicity equation,

$$\frac{Dh}{Dt} = \mathbf{v} \cdot (\boldsymbol{\omega} \cdot \nabla)\mathbf{v} - \boldsymbol{\omega} \cdot \nabla\sigma - g(q_L\zeta + \mathbf{k} \bullet \mathbf{v} \times \nabla q_L) + \boldsymbol{\omega} \cdot \mathbf{F} + \mathbf{v} \bullet \nabla \times \mathbf{F}$$

$$= \boldsymbol{\omega} \cdot \nabla L + gv\partial q_L/\partial r - gq_L\zeta + 2\boldsymbol{\omega} \cdot \mathbf{F} + \nabla \bullet \mathbf{F} \times \mathbf{v}. \tag{2.11}$$

where

$$L \equiv \frac{q^2}{2} - \sigma \equiv q^2 - B \tag{2.12}$$

defines a Lagrangian density and we have used the vector identity

$$\boldsymbol{\omega} \cdot \mathbf{F} + \mathbf{v} \bullet \nabla \times \mathbf{F} = 2\boldsymbol{\omega} \cdot \mathbf{F} + \nabla \bullet (\mathbf{F} \times \mathbf{v}). \tag{2.13}$$

We recover static energy at each time step by solving the diagnostic pressure equation

$$-\nabla^2\sigma = d_{ij}d_{ji} - \frac{\boldsymbol{\omega} \bullet \boldsymbol{\omega}}{2} + g\frac{\partial q_L}{\partial z} \tag{2.14}$$

[Bradshaw and Koh's (1981) equation with an added hydrometeor term]. In cylindrical coordinates, the rate-of-strain tensor for axisymmetric flow is

$$d_{ij} = \begin{bmatrix} \partial u/\partial r & 0.5r\partial(v/r)/\partial r & 0.5(\partial u/\partial z + \partial w/\partial r) \\ 0.5r\partial(v/r)/\partial r & u/r & 0.5(\partial v/\partial z) \\ 0.5(\partial u/\partial z + \partial w/\partial r) & 0.5(\partial v/\partial z) & \partial w/\partial z \end{bmatrix} \tag{2.15}$$

(Batchelor 1967, appendix 2). After use of (2.15) and much cancelation, (2.14) reduces to

$$-\nabla^2\sigma = \left(\frac{\partial u}{\partial r}\right)^2 + \left(\frac{u}{r}\right)^2 + \left(\frac{\partial w}{\partial z}\right)^2 + 2\frac{\partial u}{\partial z}\frac{\partial w}{\partial r} - \frac{1}{r}\frac{\partial v^2}{\partial r} + g\frac{\partial q_L}{\partial z}. \tag{2.16}$$

which is eq. (5.11) in DJ08. We solve (2.16) subject to the boundary conditions (5.12) and (5.13) in DJ08.

189 There is an alternative version of this equation. From the divergence of (2.1), (2.2) and
190 (2.8), we obtain the diagnostic equation for B, namely

191 $$\nabla^2 B = \nabla \bullet (\mathbf{v} \times \boldsymbol{\omega}) - \nabla \bullet (g q_L \mathbf{k}), \tag{2.17}$$

192 where B is related to σ through (2.4). Eq. (2.17) without the hydrometeor term was obtained
193 by Adrian (1982). In a Beltrami flow (BF), (2.17) satisfies Laplace's equation, which enables
194 B to be constant. We solve (2.16) for σ rather than (2.17) for B because the forcing function
195 in (2.16) involves only first-order derivatives and its numerical solution should be the more
196 accurate one. As shown at the end of this section and in section 4 (animation E), the reliance
197 in (2.17) of the Bernoulli function on the Lamb vector is of physical interest.

198 The initial flow in the DJ08 model before hydrometeors are introduced is a decaying
199 incompressible Beltrami flow (Shapiro 1993). This flow is defined by

200 $$\boldsymbol{\omega} = \lambda \mathbf{v} \tag{2.18}$$

201 where λ is a constant known as the abnormality. By taking the curl of (2.18) and then
202 reintroducing (2.18), we find for this flow that **v** satisfies

203 $$\nabla \times \nabla \times \mathbf{v} = \lambda^2 \mathbf{v}. \tag{2.19}$$

204 In this case, (2.1) and (2.17) reduce to

205 $$\frac{\partial \mathbf{v}}{\partial t} + \nu_e \lambda^2 \mathbf{v} = -\nabla B, \tag{2.20}$$

206 $$\nabla^2 B = 0, \tag{2.21}$$

207 which have the exact solution

208 $$\mathbf{v}(\mathbf{x}, t) = \mathbf{v}(\mathbf{x}, 0)\exp(-\nu_e \lambda^2 t), B = \text{const.} \tag{2.22}$$

209 where **v**(**x**,0) is a steady Beltrami flow that satisfies (2.19). According to (2.22), a Beltrami
210 flow decays without changing pattern.

211 By taking the scalar product of (2.18) with **v**, we obtain

212 $$h \equiv \mathbf{v} \bullet \boldsymbol{\omega} = \lambda \mathbf{v} \bullet \mathbf{v} = \lambda q^2. \tag{2.23}$$

213 This enables the definition of abnormality for general flows,

214 $$\lambda \equiv \frac{h}{q^2} \tag{2.24}$$

as devised in Part I.

In section 6, we use a control-volume method. The control volume is a surface-based cylinder of height z_c, radius r_c, and volume $V = \pi r_c^2 z_c$. For any scalar φ, we have by a vector identity and the nondivergence of $\mathbf{v}$ [see (2.2)] and $\boldsymbol{\omega}$,

$$\mathbf{v} \cdot \nabla\varphi = \nabla \cdot (\varphi\mathbf{v}), \boldsymbol{\omega} \cdot \nabla\varphi = \nabla \cdot (\varphi\boldsymbol{\omega}). \tag{2.25}$$

Let $\Sigma(\varphi)$ denote integral over time from $t = 0$ of φ, and let $<\varphi>$ denote mean value of φ in the integral over the cylindrical volume. The normal $\mathbf{n}$ is the outward normal to a closed surface as in the divergence theorem and flux of a vector refers herein to the integral over a specified surface of the normal component of the vector (i.e., not per unit area). With these definitions in mind, the fluxes per unit volume of a generic vector $\mathbf{A}$ through the specified surfaces of the cylinder are

$$\mathcal{F}_{side}(\mathbf{A} \cdot \hat{\mathbf{r}}) \equiv \int_0^{z_c} \mathbf{A}(r_c, z, t) \cdot \hat{\mathbf{r}} \frac{2\pi}{V} r_c dz, \tag{2.26}$$

$$\mathcal{F}_{top}(\mathbf{A} \cdot \mathbf{k}) \equiv \int_0^{r_c} \mathbf{A}(r, z_c, t) \cdot \mathbf{k} \frac{2\pi}{V} r dr, \tag{2.27}$$

$$\mathcal{F}_{bot}(\mathbf{A} \cdot \mathbf{k}) \equiv \int_0^{r_c} -\mathbf{A}(r, 0, t) \cdot \mathbf{k} \frac{2\pi}{V} r dr, \tag{2.28}$$

where $\hat{\mathbf{r}}$ is the unit vector in the radial direction. From (2.5), (2.25) to (2.28), (2.4), the divergence theorem and boundary conditions, the mean AM is given by

$$\langle M \rangle = \sum_{t=0}^{t} \left[\mathcal{F}_{side}(-Mu) + \mathcal{F}_{top}(-Mw)\right] + \\ + \nu_e \sum_{t=0}^{t} \left[\mathcal{F}_{side}(r\zeta - 2v) - \mathcal{F}_{top}(r\xi)\right] + \nu_e \sum_{t=0}^{t} \mathcal{F}_{bot}(r\xi). \tag{2.29}$$

From (2.11), the budget for the helicity in the control volume is

$$\langle h \rangle = \sum_{t=0}^{t} \mathcal{F}_{side}(L\xi) + \sum_{t=0}^{t} \mathcal{F}_{top}(L\zeta) + \sum_{t=0}^{t} \left[\mathcal{F}_{side}(-hu) + \mathcal{F}_{top}(-hw)\right] + \\ + \sum_{t=0}^{t} \left[\mathcal{F}_{side}(F_2 w - F_3 v) + \mathcal{F}_{top}(F_1 v - F_2 u) + \langle 2\boldsymbol{\omega} \cdot \mathbf{F} \rangle\right] + \sum_{t=0}^{t} \langle g v \partial q_L / \partial r - g q_L \zeta \rangle \tag{2.30}$$

where $\mathbf{F} \equiv (F_1, F_2, F_3)$ in component form. For the kinetic-energy budget, we obtain from (2.7)

$$\langle KE \rangle = \sum_{t=0}^{t} \left[\mathcal{F}_{side}(-Bu) + \mathcal{F}_{top}(-Bw) \right] + \sum_{t=0}^{t} \langle \mathbf{v} \cdot \mathbf{F} - g q_L w \rangle \,. \tag{2.31}$$

By forming the volume mean of (2.17) and using Green's theorem, we obtain for all time,

$$\langle \nabla^2 B \rangle = \mathcal{F}_{side}(\mathbf{v} \times \boldsymbol{\omega} \cdot \hat{\mathbf{r}}) + \mathcal{F}_{top}(\mathbf{v} \times \boldsymbol{\omega} \cdot \mathbf{k}) + \mathcal{F}_{bot}(g q_L) - \mathcal{F}_{top}(g q_L). \tag{2.32}$$

Because $\mathbf{v}\times\boldsymbol{\omega}\bullet\mathbf{k} = 0$ at $z = 0$ follows from the model's boundary conditions, there is no flux of Lamb vector at the ground.

3. Methodology

The basic simulation (EXP011) in DJ08 (see his section 6) was rerun to evaluate many significant quantities such as angular-momentum advection and terms in the helicity equation (2.11) and kinetic-energy equations (2.7). The diagnostic equation (2.16) for static energy, σ, was solved at every time step and the Bernoulli function, B, was then obtained via (2.8). Four-panel animations using time-invariant contour levels were used to visualize the evolution of 31 fields (see section 4). These animations allow better interpretations of the EXP011 simulation than those presented in DJ08 using snapshots.

Trajectories calculations are another new feature of the model reuse. Forward trajectories were computed using Petterssen's method (Siebert 1993). The trajectory code was tested on a simulation without hydrometeors. In this case, the trajectories successfully followed the streamlines of the decaying Beltrami flow (Fig. 1). Ascent into the updraft is broad. Parcels acquire rotation about a vertical axis only as they are rising (Davies-Jones 1982) so there is little rotation near the ground.

By trial and error, I found the initial position of a parcel P (more precisely a ring of parcels since the flow is axisymmetric) that enters the tornado at a low height at $t = 5.6$. This parcel has the same starting position as the one for Beltrami flow in Fig. 1, but follows a much different path that takes it close to the ground and axis as required for tornado formation. Section 5 describes how various properties of P such as AM, helicity and KE evolve along the trajectory of this parcel. Gridded fields were interpolated bilinearly to obtain values at the parcel location. The trapezoidal rule was used to temporally integrate these properties along the trajectory. Finally, we adopted a control-volume approach in

section 6 to evaluate mean quantities within and imports into a cylinder that tightly encloses the eventual tornado.

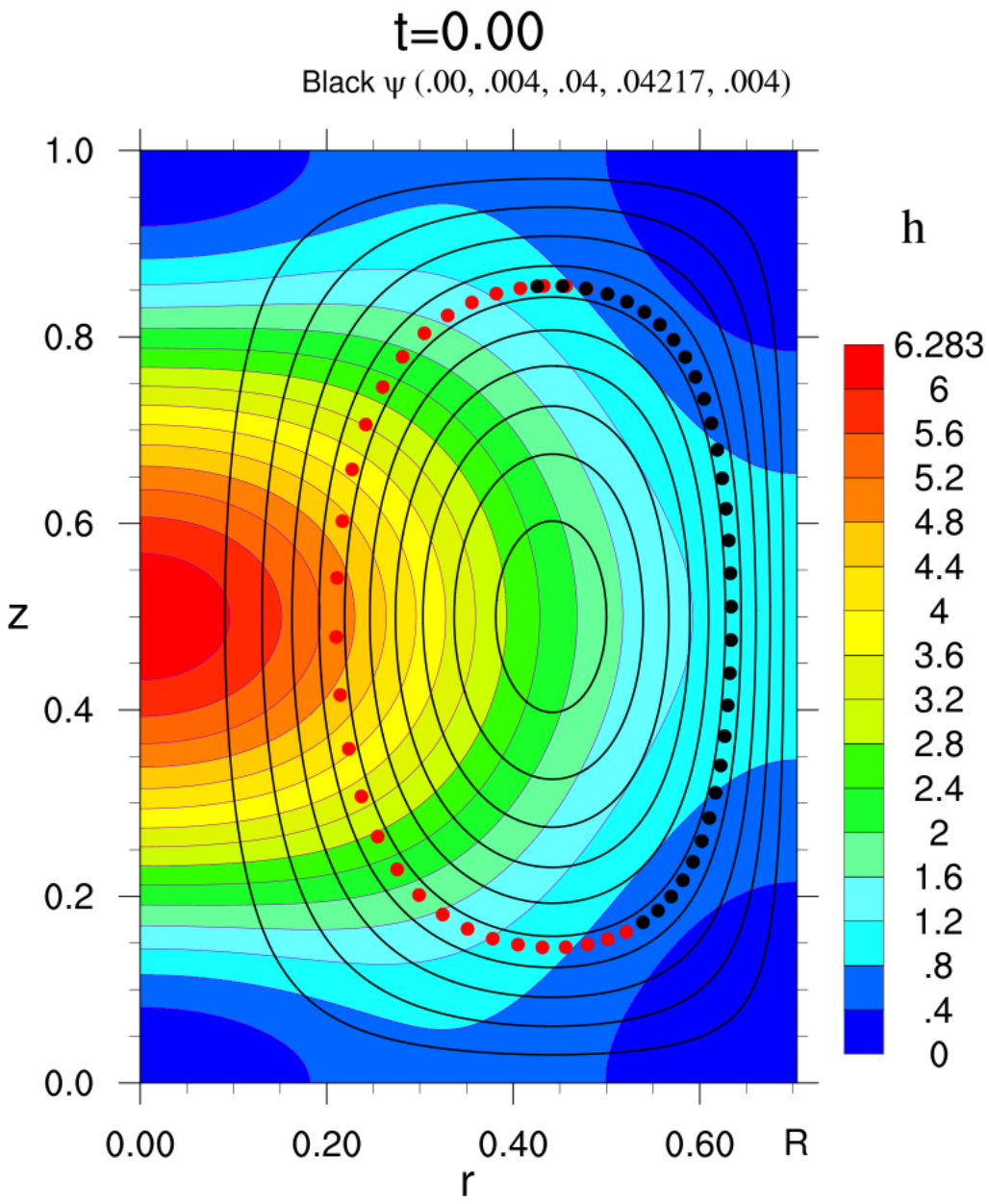

Fig. 1. The trajectory from $t = 0$ to $t = 6$ of a parcel in the decaying Beltrami flow. Initially, the parcel is at (.4257, .8542). The black unfilled contours are the streamlines and the filled contours are for helicity density h. The values are the initial values. The streamlines are also contours of AM. By t =6, the streamfunction and helicity fields have decayed by 11% and 21%, respectively, in amplitude without changing shape. The flow direction is clockwise in this depiction. Black and red dots represent the position of the parcel at time intervals of 0.1 from $t = 0$ to $t = 3$ and $t = 3.1$ to $t = 6$, respectively. Coincidence of the trajectory with an initial streamline verifies the trajectory calculation.

4. Animations of fields

To aid physical interpretation of the numerical solutions, I animated the evolutions of 30 fields. Each animation contains four panels. Table 1 lists the variable(s) plotted in each panel of each animation.

Animation	Panel 1	Panel 2	Panel 3	Panel 4
A	u	v	w	ψ and M
B	h and ψ	KE	L and M	σ
C	$-\mathbf{v}\bullet\nabla M$	ξ	η	ζ
D	$-\partial\sigma/\partial r$	v^2/r	$-\partial\sigma/\partial z - gq_L$	$-\partial\sigma/\partial r+v^2/r$
E	$r\mathbf{v}\bullet\boldsymbol{\omega}$	$-B$	$\mathbf{k}\bullet\mathbf{v}\times\boldsymbol{\omega}$	$\nabla^2 B$
F	$-\mathbf{v}\bullet\nabla\sigma$	$-\mathbf{v}\bullet\nabla B$	$\mathbf{v}\bullet\mathbf{F}$	$-gq_L w$
G	h_{kin}	h_{gen}	h_{drag}	h_{fric}

Table 1. Variables in panels 1 (top left), 2 (top right), 3 (bottom left) and 4 (bottom right) of each animation. Additionally, the hydrometeor mixing ratio is overlaid on one or two panels in almost all the animations.

The simulation starts with the Beltrami flow described in section 1. Without hydrometeors, the BF simply decays exponentially without changing pattern. The decay rate of the velocity and vorticity components, M, and all linear quantities except for static energy and its derivatives decay at the rate $-\nu_e\lambda^2/Re$ where $Re = 2000$ is the Reynolds number and $\lambda = 2\pi$ is the abnormality. Static-energy and its gradients and all quadratic quantities such as helicity decay at twice this rate. The evolution of a variable amplitude in BF is visualized by looking at the first frame of each animation for its pattern and factoring in its decay in amplitude at the applicable rate.

Tornadogenesis occurs after hydrometeors are allowed to fall from the part of the top boundary that is above the updraft. For reference, the 1.5 and 3.5 g kg $^{-1}$ contours of hydrometeor mixing ratio are overlaid on several panels of the animations. Contour values in filled and unfilled contour plots are supplied in label bars and information labels, respectively. For fields plotted with unfilled contours, information labels enclose in parentheses the minimum value of the field, the minimum contour value, the maximum contour value, the maximum value of the field, and the contour interval. Non-negative and negative contours are solid and dashed, respectively. The zero contour is made thicker for easy recognition. In fields that are zero initially, the zero contour is usually omitted because it is ill-defined at small times. The contour lines are purple in filled-contour plots, and either black or white in unfilled-contour plots. For fields with filled contours, the minimum and maximum values are supplied above the plots, and the locations of the global maxima or minima (which one is most relevant for the particular field) are marked by circled crosses (which are partly hidden when they lie on a boundary). The moving dot in the animations traces the trajectory of a parcel that enters the tornado. Although the starting points of this parcel and the parcel, whose path in Beltrami flow is depicted in Fig. 1, are the same, their final locations are very different.

Animation A

Animation A shows the evolution of the hydrometeor q_L, wind (u, v, w), streamfunction ψ and angular momentum M. Since M serves as a Stokes streamfunction for ξ ($= -\partial M/r\partial z$) and ζ ($= \partial M/r\partial r$), the M contours are projections of vortex lines onto a radial-height plane.

The hydrometeors fall in an annular curtain near the updraft–downdraft interface. The associated drag force causes the angular momentum contours to separate from the streamlines and the Beltrami flow to become unbalanced. As the rain curtain extends downward, it causes a secondary downdraft near the updraft edge and flow modifications that proceed slowly at first but later on change extremely rapidly. By constricting the updraft, this downdraft prevents air from rising gently into a wide updraft as is the case in the initial Beltrami flow. Instead, air turns upward more abruptly into a narrower updraft base.

During tornadogenesis, AM is transported inward towards the axis and downward. Convergence at low heights of the updraft also increases. Amplified tilting and stretching of

enhanced vorticity produce faster updraft rotation at lower levels. The streamlines turn upward more abruptly as they enter the rotating updraft. Ultimately, low-level air that has descended with adequate AM penetrates close to the axial updraft where it is stretched vertically in strongly convergent flow and spins up into a tornado. Note that the air with the most AM (> 0.200) stays aloft between 3 and 9 km AGL throughout the simulation. Owing to diffusive loss of AM, the parcel P crosses the AM contours towards lower values. This is particularly evident when the parcel is close to the ground.

In this experiment, the evolution of the near-surface flow from mesocyclone to QT to tornado is due to a continuous process of downward and inward AM advection associated with low-level convergence near the axis. This convergence is enhanced by outflow from the rainy downdraft and by frictionally induced cross-isobaric flow. The radii of maximum tangential wind and maximum surface inflow decrease steadily between $t = 4$ and $t = 6$ even though these parameters pertain sequentially to the mesocyclone, the QT, and the tornado (DJ08). Thus, low-level mesocyclogenesis and tornadogenesis are consequences of a single mechanism (as in Lewellen and Lewellen 2007a, p. 2188). The near-ground mesocyclone is just a passing phase as the flow collapses into a tornado. Eventually, two vortices coexist, one that builds downward along the axis from midlevel and one that develops later from the ground upwards. The two vortices are the mesocyclone/QT aloft with maximum strength increasing and lowering from 6 to 3 km between $t = 4$ and 6; and a tornadic vortex that forms from the ground up at $t = 5.4$ and peaks at $t = 6.1$. The two vortices are coupled at a vortex breakdown aloft, which arises because upstream and downstream conditions are incompatible with a smooth variation. Instead, there is an abrupt transition from supercritical to subcritical flow. In the supercritical flow below the breakdown, waves are unable to propagate upstream so the flow in the axial jet is unaware of conditions above the breakdown.

We now examine the flow evolution more precisely. At $t = 3.7$, the curl of the hydrometeor drag force generates positive (negative) azimuthal vorticity on the inward (outward) side of the curtain (see animation C), causing the minimum vertical velocity to move inward from the side and an inflow maximum to form on the updraft–downdraft interface just inward of the rain curtain at a height $z = 0.3$. The updraft width, as measured by the radius of the $w = 0$ contour, contracts at low levels owing to the intrusion of subsiding outflow from the rainy downdraft. This undercutting of the updraft by outflow results in considerable spreading of the updraft with height. In response to the ‘squeezing’ of the low-

357 level updraft and near-conservation of AM, the tangential-velocity maximum moves
358 downward as AM is advected downward and inward. These developments mark the
359 beginning of the collapse of the mesocyclone.

360 At t = 4.3. the minimum of u at the surface is once again the global minimum of u. The
361 maximum of w is still on the axis but has lowered slightly. The maximum of v has moved
362 inward as the updraft continues to contract at low heights.

363 At t = 4.8, there is still only a single vortex, a mesocyclone that continues to contract and
364 intensify. The maximum surface-inflow velocity has increased and moved inward. The
365 downdraft has further constricted the updraft. In the atmosphere, this downdraft
366 encroachment is visible as a clear slot and as cloud elements cascading down the side of the
367 storm tower.

368 By t = 5.1, the mid-level vortex has contracted into a QT aloft. Its maximum tangential
369 wind is approaching the speed limit.

370 Around t = 5.3, the maximum of vertical velocity drops down the axis to z = 0.1 and a
371 secondary maximum in tangential velocity forms near the ground. Note that the global
372 maximum of tangential velocity does not descend steadily from aloft all the way to the
373 ground. Instead, it jumps to near the ground as the lower maximum forms and quickly
374 exceeds the original maximum. The vertical velocity is still upward all along the axis with a
375 maximum that is still near the speed limit. The downdraft has penetrated further into the
376 updraft at low levels and brought air with modest AM even closer to the foot of the axis. The
377 maximum inward surface velocity and minimum surface pressure continue to move inward
378 and intensify.

379 At t = 5.4, the low-level tangential-vorticity maximum intensifies as a tornado forms. It
380 is an end-wall vortex with an axial jet that is capped by a vortex breakdown, an abrupt
381 transition to the broader QT aloft. The maximum updraft is now located in the axial jet. The
382 speed limit is exceeded significantly only in the axial jet. The axial flow immediately above
383 the breakdown is reduced but still upward at this time. Downdraft is present very near (2 km
384 from) the tornado as observed in Doppler-radar and photogrammetric analyses (Davies-Jones
385 1986).

386 An axial downdraft begins at mid to upper levels just before $t = 6$. The upper half of the
387 updraft turns to downdraft in response to large downward axial pressure-gradient force aloft.
388 This is the model counterpart of collapse of the overshooting top in supercells.

389 At $t = 6.1$, the tornado is at its peak. At low heights, the intruding downdraft constricts
390 the updraft to the tornado itself (DJ08). The resulting upward velocity is tremendous because
391 the mass transported in the updraft aloft has to pass through the constriction of the axial jet.
392 The high-speed updraft in the tornado is often visible to observers. At the surface, radial flow
393 into the corner region is 1.53 (51 m s^{-1}). Vertical and tangential winds in the axial jet now far
394 exceed the speed limit of 1 (the initial maximum updraft speed), reaching speeds of 3.49 (116
395 m s^{-1}) and 2.27 (76 m s^{-1}), respectively, while the tangential wind in the QT aloft stays
396 roughly at the limit. The nondimensional extreme tangential speed v_m and vertical speed w_m
397 are comparable to the theoretical values for the end-wall vortex deduced by Fiedler and
398 Rotunno (1986) and values for some numerically simulated vortices (Lewellen et al. 2000).

399 After t = 6.1 (not shown), the tornado fills from above as there is no 'buoyant cork'
400 (DJ08). The axial downdraft reaches the surface at $t = 7$ as the tornado dies.

401

402 *Animation B*

403 Animation B shows the evolution of the local kinetic energy, $q^2/2$, the static energy σ,
404 helicity density (hereafter shortened to helicity) h, abnormality λ, and L (kinetic energy
405 minus static energy) fields. Streamfunction and AM fields are superposed on the helicity and
406 L fields, respectively, to reveal where helicity is being advected and generated.

407 Initially the maximum KE is located at the midpoint of the updraft. At $t = 4.2$, a new
408 global maximum forms at mid height and halfway between the axis and the updraft edge. As
409 the tornado forms at $t = 5.4$, a new global maximum of KE develops in the axial jet and
410 rapidly intensifies. The maximum aloft lowers to just above the vortex breakdown and is
411 associated with the QT aloft.

412 The minimum of static energy, σ, is initially -0.5 and is located on the axis at mid
413 height. At $t = 4$, σ starts to fall at low heights. The minimum begins a slow descent in
414 response to constriction of the updraft and downward and inward advection of AM. By $t =$
415 5.1, an inflow low (Barnes, 1970; Davies-Jones and Brooks 1993; Davies-Jones 2002) is now

evident in the surface σ field. It is coincident with the maximum surface inflow. The free-slip lower boundary condition on radial velocity allows considerable inflow along the surface. Because of the tendency for σ on a streamline to decrease as the velocity increases and vice versa (Bernoulli's principle), the lowest σ at the surface (an inflow low) is nearly collocated with the maximum in surface inflow all through the simulation (even when a tornado is present). A $t = 5.3$, a new σ minimum develops at low height and becomes the global minimum as the tornado forms ($t = 5.4$). This low deepens rapidly. At $t = 6.1$, the axial σ deficit in the axial jet is very large. Fiedler and Rotunno (1986) assumed that Bernoulli's principle held approximately in the axial jet. This is a good assumption as the Bernoulli effect ($w_m^2/2 = 6.09$) accounts for 93% of the extreme σ deficit $\Delta\sigma$ of 6.54 (Δp = 83 mb) in the axial jet. In contrast, the flow above the vortex breakdown is roughly cyclostrophic and so the axial σ deficit there is proportional to v_c^2 where v_c is the maximum tangential velocity in the QT aloft.

We may also explain the low pressure in the vortex from the perspective of the diagnostic equation for σ (Bradshaw and Koh 1981). As a general rule, a variable is negatively correlated with its Laplacian. Since $d_{ij}\, d_{ji} \geq 0$ and $\boldsymbol{\omega}\bullet\boldsymbol{\omega} \leq 0$ in (2.14), there is a tendency for low static energy to occur in regions where the vorticity dominates the rate of deformation (as in the vortex) and for high static energy to be present where the rate of deformation is dominant (as near a stagnation point). In the simulation, the lowering of static energy is roughly coincident with increasing vorticity. Incidentally, owing to cancellation on the right side of (2.14), the diagnostic equation for σ, (2.16), is independent of the radial vorticity $-\partial v/\partial z$.

The helicity field is initially equal to $2\pi q^2$ with a maximum value of 2π located half way up the axis. At $t = 3.2$, a patch of negative helicity develops in the outer part of the rain curtain. At $t = 3.8$, the global maximum of h relocates towards the side of the updraft and lowers slightly. The isopleths around this maximum then extend downward. A new global maximum forms on the ground at $t = 5.2$. As the tornado forms, the new maximum then moves into the axial jet. Between $t = 5.4$ (the time of tornado formation) and 6.1 (the time of maximum intensity), the maximum helicity increases rapidly from 38 to 724. Outside the tornado there is a large patch of weak to moderate negative helicity.

Note that parcels such as P (located by the dot) that enter the tornado do so by traveling downward from a great height near the side of the closed domain before turning and flowing almost along the ground into the tornado. They are able to follow this path because the flow is unstratified (to avoid the complications of gravity waves). In a more realistic model, parcels would flow horizontally into the storm from a stably stratified environment. The original high locations of parcels that enter the tornado are of little consequence to the helicity dynamics because the helicity of P is less than one until $t = 4.5$, at which time the parcel is low to the ground and halfway to the axis. The helicity of P increases extremely rapidly as the tornado forms and intensifies, reaching a value of 100 at $t = 6.1$ (see section 5).

By definition, the generalized abnormality λ equals the helicity density h divided by q^2. Initially it is a constant field equal to 2π. It becomes indefinite at stagnation points so it flagged as missing wherever q^2 is tiny ($< 10^{-3}$). Large values of λ first develop in boundary layers near the $(r, z) = (R, 0)$ stagnation point at around t = 3.3, then spread along the ground, and upward into the tornado. Values greater than 50 occur in a shallow layer next to the ground and in the tornado itself.

The L field is important because the term $\boldsymbol{\omega} \bullet \nabla L$ is the greatest generator of parcel helicity in the helicity equation (2.11). Initially L has a maximum value of one at the mid height of the axis. At $t = 5.3$, the global maximum of L suddenly drops to near the ground. As the tornado forms and intensifies, the maximum value increases to 13 at $t = 6.1$. From the displayed M and L contours, it is evident that $\boldsymbol{\omega} \bullet \nabla L$ becomes large in the surface inflow layer of the tornado. This generation of helicity is mitigated locally to some extent by helicity advection.

Animation C

This animation reveals the evolution of AM advection and the vorticity components ξ, η, and ζ. The descent of the rain curtain causes AM to be advected downward, then inward and subsequently upward in the updraft. From $t = 0.4$ to 2.5, the paths of the maximum AM advection and parcel P are close together. From $t = 3$ to 4, the maximum increases in value significantly and moves into the updraft at lower mid heights. At $t = 4.4$, the maximum jumps down to $z = 0.1$. It then moves inward and intensifies as it enters the tornado.

476 The initial vorticity features a maximum of vertical vorticity on the axis at the mid height,
477 a maximum of tangential vorticity, η, inside the updraft edge at the mid height, and a
478 minimum of radial vorticity, ξ, at the ground below the η maximum. The updraft and
479 downdraft have cyclonic and anticyclonic vorticity, respectively.

480 The curl of the hydrometeor drag force creates new centers of azimuthal vorticity as the
481 flow in (r, z) planes becomes more curved and sheared. At t = 2.2, the global maximum of η
482 shifts to the rain curtain. At t = 4.5, it shifts again to a low height in the updraft. It then
483 intensifies as it moves further inward and downward. It eventually ends up in the corner
484 region of the tornado where it is associated with the abrupt upward turning of the stream
485 surfaces.

486 From t = 4.5 onward, the minimum in radial vorticity moves steadily inward along the
487 ground and deepens. As the tornado forms, the minimum is capped by a maximum of ξ
488 associated with the tangential velocity decreasing with height above its low-level maximum.

489 As the original maximum in vertical vorticity fades away, a new maximum forms off axis
490 in the updraft at a lower height at around t = 3.8. It slowly strengthens until t = 5.2 when it is
491 replaced by a new maximum that then moves inwards and downwards into the axial jet while
492 intensifying rapidly. Most of the downdraft has anticyclonic vorticity. Surprisingly the
493 vertical vorticity of the parcel P is anticyclonic until t = 5.4. It changes sign as P crosses the
494 trough in the M-field (where $\partial M/\partial r = 0$) in animation B. In this model there is no flow of
495 cyclonic vertical vorticity into the tornado from afar. At this time, P is still in downdraft
496 (animation A). At t =5.5, P is just past its lowest point and its vertical vorticity is cyclonic,
497 an indication that the tornado is getting stronger. Davies-Jones (2025c) showed theoretically
498 and from further results from the DJ08 model that the presence of cyclonic vorticity at the
499 nadir of trajectories of tornado-bound parcels is associated with inward advection of angular
500 momentum that acts to intensify the vortex against the retarding effects of diffusion.

501 Why is the tornado surrounded by anticyclonic vorticity? First note that baroclinic
502 vorticity is generated as azimuthal vorticity by drag-associated torques, but remains in this
503 component because the axisymmetry prohibits tilting of azimuthal vorticity. At a fixed
504 height, the areal average of the vertical vorticity ζ ($=\partial M/r\partial r$), is zero because M = 0 at the
505 side. Thus, increasing cyclonic vorticity at a low elevation must be accompanied by weaker
506 but more widespread anticyclonic vorticity at the same level. This constraint is satisfied
507 because the intensifying cyclonically revolving downdraft is wider and still primarily

anticyclonic. The penetration of this downdraft toward the axis surrounds the vortex with anticyclonic vorticity in a "clear slot." This vorticity is tilted radially inward in the inward-directed outflow from the downdraft and then turned abruptly upward in the axial updraft. Low-level spin-up results from stretching of this cyclonic barotropic vorticity.

Animation D

Animation D presents the following forces: the sum of the vertical pressure-gradient force (VPGF) plus the drag force $-gq_L\mathbf{k}$, (VPGF+ ≡ VPGF $-gq_L\mathbf{k}$), the radial pressure-gradient force (RPGF), the centrifugal force (CF), and the cyclostrophic imbalance (CI ≡ RPGF + CF). The boundary conditions on u, v, w and the equations of motion dictate that RPGF = CF = CI = 0 at $r = 0$, R and VPGF+ = 0 at $z = 0$, 1 (DJ08).

In the Beltrami flow (see first frame), VPGF is positive and negative in the lower and upper halves of the domain, respectively, with maximum and minimum values on the axis. The cyclostrophic imbalance is positive throughout almost all of the updraft. This arrangement of forces gives rise to trajectories such as the one shown in Fig. 1. In the lower half of the domain, the upward VPGF changes descent at large radii into broad ascent within the updraft, while the cyclostrophic imbalance provides radial acceleration towards the updraft and deceleration within it. At the ground, the RPGF decelerates the surface inflow beneath the updraft. The resulting flow resembles a midlevel mesocyclone. Virtually none of the inflowing air penetrates close to the axis before rising so strong winds and significant AM close to the ground are absent.

Tornado formation requires a completely different configuration of forces. Subsiding parcels should experience just enough upward VPGF+ to enable them to level off near the ground. Similarly, they should experience negative CI that accelerates them inward until they nearly reach the axis where mass conservation dictates that they ascend rapidly in a jet..

A curtain of hydrometeors eventually changes the force patterns from the Beltrami situation to the tornadogenesis one. Around t = 3.6, the region of positive RPGF that prevents inflowing air from getting close to the bottom of the axis starts contracting. Simultaneously, a pocket of negative CI forms near the updraft edge. It intensifies and moves inward together with the updraft edge. Lower values of VPGF+ begin penetrating

538 inwards at low levels. Also, the VPGF+ maximum on the axis starts moving downward
539 along the axis and intensifying.

540 At t = 4.6, parcel P begins to be accelerated towards the axis by negative CI. It is
541 undergoing weak upward acceleration to slow its downward momentum. P stays in the
542 pocket of negative CI until it rises in the tornado at t = 5.5. This pocket is responsible for
543 low-level penetration of parcels close to the axis and subsequent spin up of the tornado.

544 The maximum of VPGF+ continues to move downward and ends up in the axial jet. At
545 the time of maximum tornado intensity (t = 6.1), the maximum and minimum vertical
546 accelerations are 1.95g in the axial jet and −0.73 g in the QT just above the axial jet.

547

548 Animation E

549 Animation E shows the Bernoulli function B (the sum of KE and static energy), the
550 forcing function, $-\nabla^2 B$, for the diagnostic B equation, and the radial and vertical components
551 of the Lamb vector. The azimuthal component of the Lamb vector is equal to the advection
552 of AM (section 2).

553 In the initial Beltrami flow, B is a constant, which is set to zero. Generally, B is small
554 compared to $q^2/2$ and the static energy is given approximately by the Bernoulli principle
555 wherein low static energy associate with large KE and vice-versa. However, $-B$ becomes
556 substantial above the vortex breakdown and significantly exceeds KE there. More explicitly,
557 the minimum of B lies in the range $(-0.1, 0)$ for $t \le 4.2$. By $t = 4.3$, lower values have
558 developed in the updraft at mid heights. Between $t = 4.3$ and the time of tornado formation,
559 the forms minimum deepens as it descends to $z = 0.2$ (a height just above the vortex
560 breakdown) and moves inward to very near the axis. As the tornado intensifies, the minimum
561 deepens further from −0.5 to −1 while barely moving. The parcel P suffers significant loss of
562 Bernoulli function as it enters and ascends to $z = 0.2$ in the tornado.

563 In (2.17), $\nabla^2 B$ equals $\nabla\bullet(\mathbf{v}\times\boldsymbol{\omega})$ plus the hydrometeor term, $g\partial q_L/\partial z$. The hydrometeor
564 term is significant at small times because it upsets the equilibrium of the initial Beltrami flow,
565 in which the Lamb vector is zero and B is constant. After significant Lamb vectors are
566 generated, the divergence of the Lamb vector becomes the dominant term. At later times, the
567 fields of $\nabla^2 B$ and $\nabla\bullet(\mathbf{v}\times\boldsymbol{\omega})$ are nearly equal and the hydrometeor term becomes negligible.

Lamb-vector convergence values become sizeable in the updraft near $(r, z) = (0.15, 0.4)$ at around t =4.6. These higher values then extend upward and downward and move inward. They provide the forcing for the large deficit of B in the tornado as Lamb-vector convergence forces low B. If we imagine a cylindrical control volume of radius 0.07 and height 0.1 that contains the lower part of the tornado (when present), then according to (2.32) applied at later times when the water loading terms are insignificant, the average $\nabla^2 B$ is equal to the sum of the exports of Lamb vector through the side and top of the cylinder. As the tornado is forming and intensifying, $\nabla^2 B$ is well correlated with $-B$ so loss of B in the tornado should associate with net export of Lamb vector. This is indeed the case because, as shown in the animation and in section 6, the export of the radial component of Lamb vector through the cylinder's side ($r = 0.07$, $z \le 0.1$) exceeds the import of Lamb vector at its top ($r \le 0.07$, $z = 0.1$).

On a different topic concerning B, the surface-inflow minimum ($u_{\min} < 0$) in the Beltrami flow is stationary and slowly fills owing to viscous decay. The following analysis from DJ08 describes the force imbalance needed for this minimum of u to move inward and deepen as it does during corner flow collapse (Lewellen and Lewellen 2007b). At the ground, there is no centrifugal force because of the no-slip condition on v and so $\partial u/\partial t = -\partial B/\partial r + \mathrm{Re}^{-1}(\nabla^2 u - u/r^2)$ where $B = \sigma + u^2/2$, etc., are surface values here. The radial friction force is relatively small and has a maximum near the u minimum. Thus, it has little influence on the motion of the minimum. Then the minimum deepens if $\partial B/\partial r$ is positive at its center and it moves inward if $\partial^2 B/\partial r^2 < 0$ there. These surface conditions occur quite near the axis after $t = 4.3$.

Animation F

This animation supplies the terms in the KE-tendency equations (2.6) and (2.7). In (2.7), the local rate of KE change is initially due to the work done by friction, $\mathbf{v}\bullet\mathbf{F}$ (< 0). The work performed by the hydrometeor drag force stays small throughout the simulation. From t = 4 until near the time of maximum tornado strength, the $-\mathbf{v}\bullet\nabla B$ term is the dominant one. At the peak of tornado intensity, $\mathbf{v}\bullet\mathbf{F}$ nearly negates $-\mathbf{v}\bullet\nabla B$ in the axial jet.

In (2.6), the work done by the pressure-gradient force is the predominant production term. Locally, advection of KE cancels much of this production of KE.

598

599 Animation G

600 The terms in the helicity equation (2.11) are presented in this animation. The terms on
601 the right of this equation are the helicity generation tendency ($h_{gen} = \boldsymbol{\omega}\bullet\nabla L$), and the helicity
602 tendencies due to hydrometeor drag, (h_{drag}) and friction (h_{fric}). The local rate of change of
603 helicity equals the sum of these terms plus the advection term, $h_{adv} = -\mathbf{v}\bullet\nabla h$. Both h_{gen} and
604 h_{adv} get very large but largely cancel one another. Therefore, we define a kinematic helicity
605 tendency term h_{kin} as $h_{gen} + h_{adv}$. In the initial Beltrami state, h_{kin} and h_{drag} are both zero and
606 h_{fric} is negative.

607 From $t = 1.2$ to 3.3, h_{drag} has the largest maximum value. From $t = 3.5$ to 6.0, h_{kin} is
608 significantly larger in magnitude than h_{fric}. The maximum helicity first exceeds the initial
609 maximum helicity at $t = 4$ (animation B). Subsequently, the maximum helicity increases
610 rapidly due to helicity production by the h_{kin} term. At $t = 4$, the global maximum of h_{kin} is
611 situated in the updraft at mid height and halfway between the axis and the updraft edge. At t
612 = 4.7, it relocates to near the ground. It then shifts to the ground before moving inward and
613 upward into the axial jet. As the tornado attains maximum intensity at $t = 6.1$, helicity loss in
614 the axial jet balances helicity production there by h_{kin}.

615

616 **5. Tornadogenesis from a parcel perspective**

617 Consider the parcel P that has the trajectory outlined by the moving dot in the animations.
618 This parcel enters the tornado at the point S = (.0432, .0576) at time $t = 5.6$. Initially, P is at
619 (.4257, .8542). Fig. 2 provides its coordinates versus time. The parcel travels downwards
620 near the outer rim and then inward at low levels. It passes underneath the rainy downdraft
621 just before outflow from this downdraft blocks radial inflow from large radii. Therefore, the
622 tornado is not forming according to the recycling hypothesis (Fujita 1983, 1985) as
623 conjectured by DJ08.

624

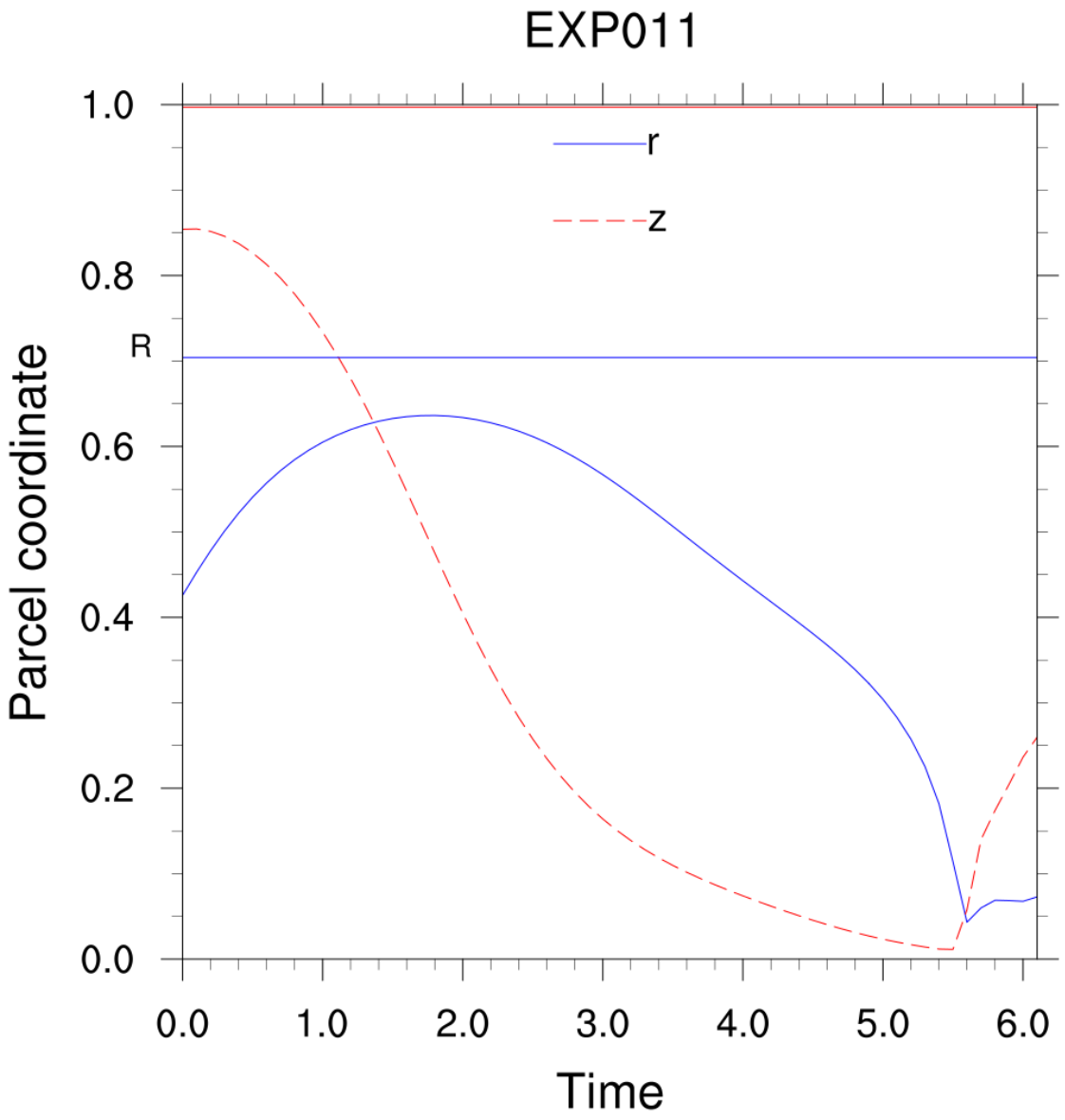

Fig. 2. The r and z coordinates of the parcel P. The blue and red straight lines at $r = R$ (=.7042) and $z = 1$ represent the side and top of the domain.

AM is conserved in the absence of viscous diffusion. The parcel P starts out with about half of the domain-maximum AM. The parcel loses 60% of its AM before entering the tornado. Since the greatest rate of loss occurs after $t = 4$ when P is close to the ground (Fig. 3), the loss of AM is mainly due to diffusion in the ground boundary layer.

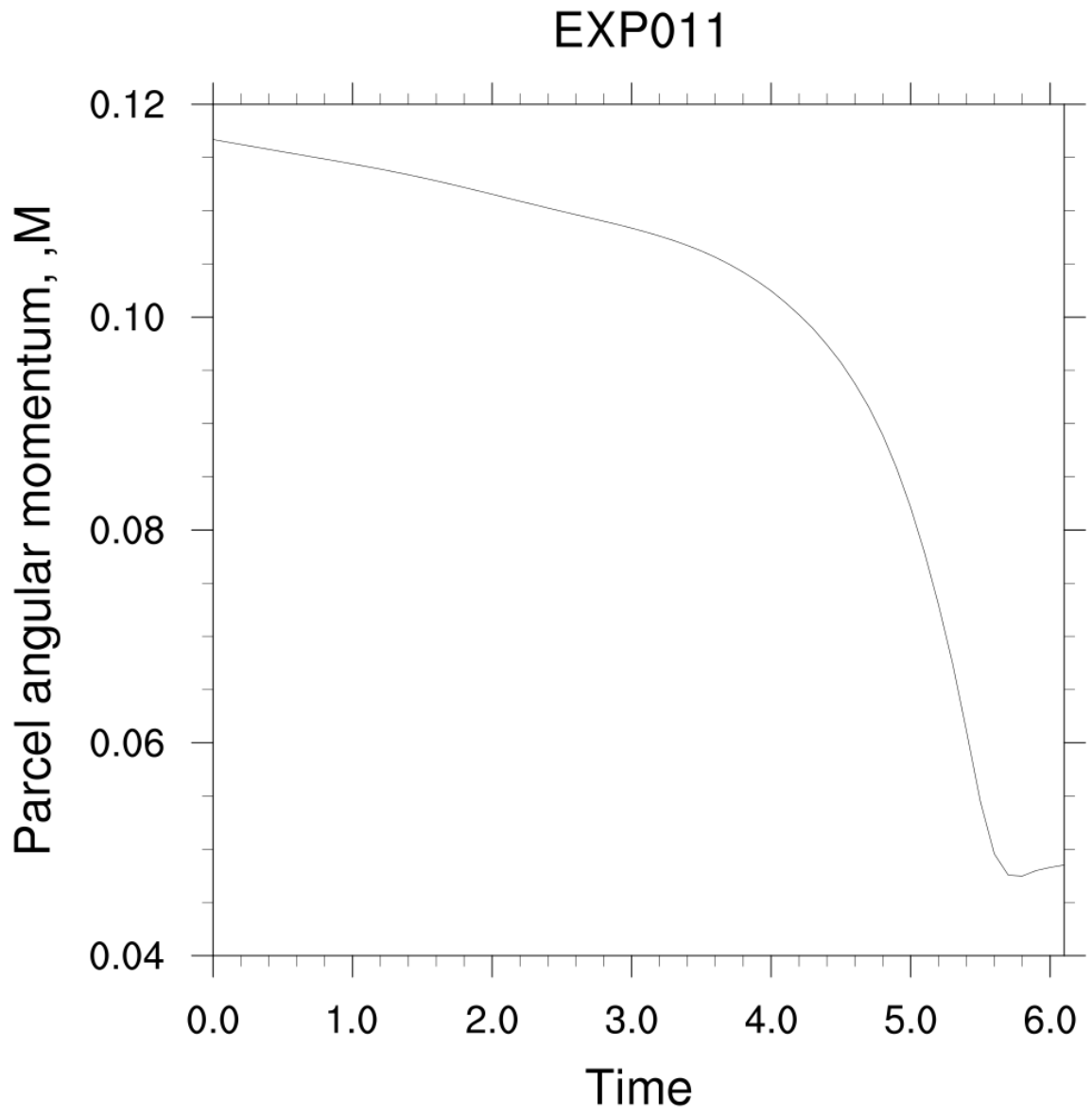

634

635 Fig. 3. The angular momentum of P as a function of time. AM loss is entirely due to diffusion.

636

637 Despite the decline in the parcel's AM, its tangential velocity increases very rapidly in the
638 time interval from 5.4 to 5.6 (Fig. 4). This increase is due to the parcel's close approach to
639 the axis.

640

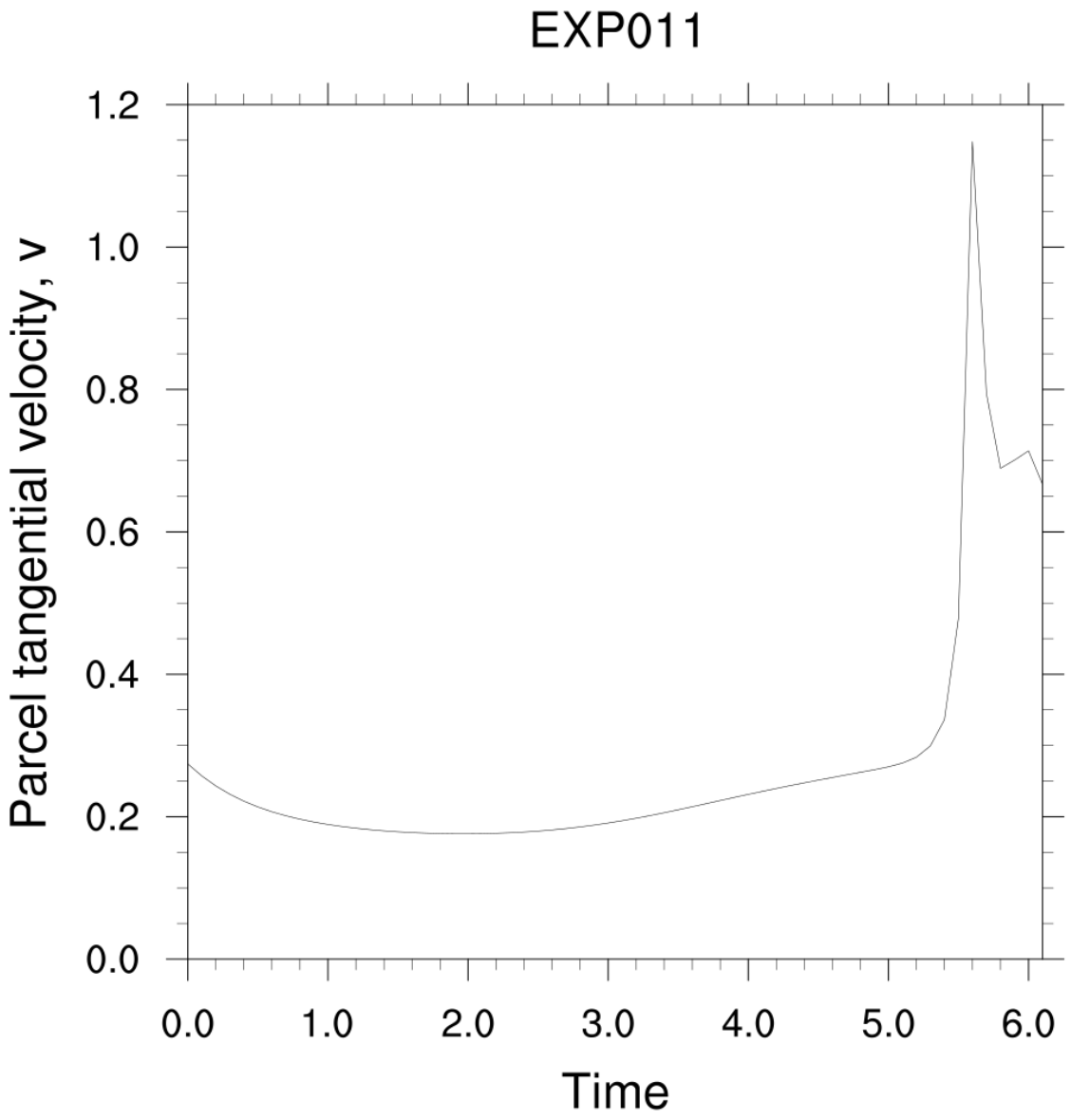

641

642 Fig. 4. Azimuthal velocity of P as a function of time.

643

644 Fig. 5 shows the evolution of the parcel's helicity and the helicity gains due to terms in
645 the helicity equation (2.11) as functions of time. (Note that there is no advection term for a
646 moving parcel). There is a hundredfold increase in the helicity of P. The gains in parcel
647 helicity start a few minutes prior to the parcel entering the tornado and are due to the effects
648 of the $\int \boldsymbol{\omega} \bullet \nabla L dt$ term. The friction terms provide minor losses. The accumulated
649 hydrometeor-drag effect is negligible because the parcel is in the rain curtain for only a short
650 time. The computational error is insignificant. Note that in dry, inviscid and homentropic

651 flow, the gain in helicity would be $\omega \bullet \nabla \Phi$ (see eq. 3.25 in Part I). This term proved too
652 difficult to determine from model data.

653

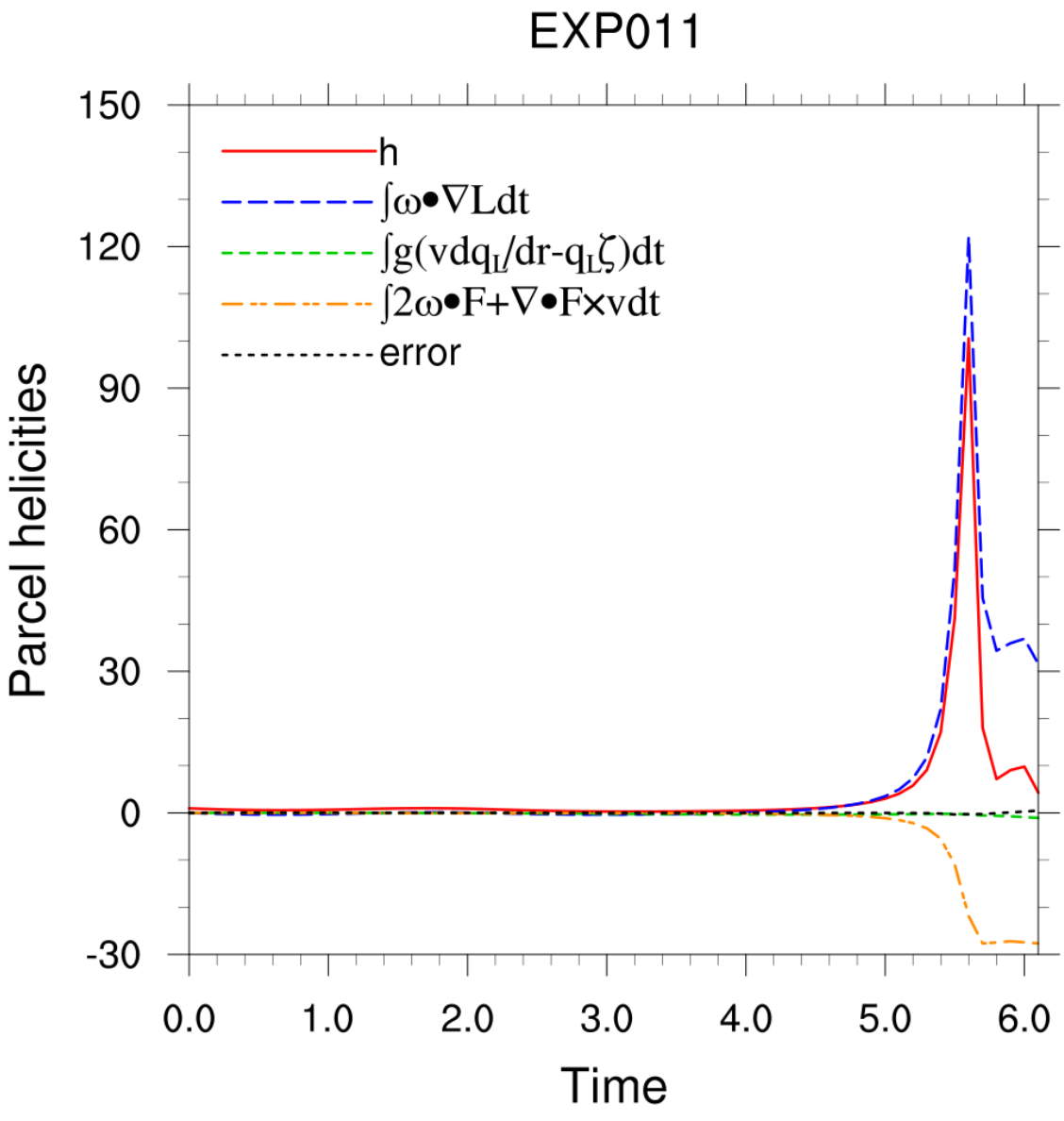

654

655 Fig. 5. Parcel helicity and integrals from $t = 0$ to t of terms in (2.11) as functions of time. Each
656 colored curve is the integral following parcel P of the term with the same color in (2.11).

657

658 The abnormality of the parcel (Fig. 6) remains at or below its initial value of 6.28 until $t =$
659 4. It then increases to its maximum value of 44 at t =5.4, the time that the tornado forms.

660

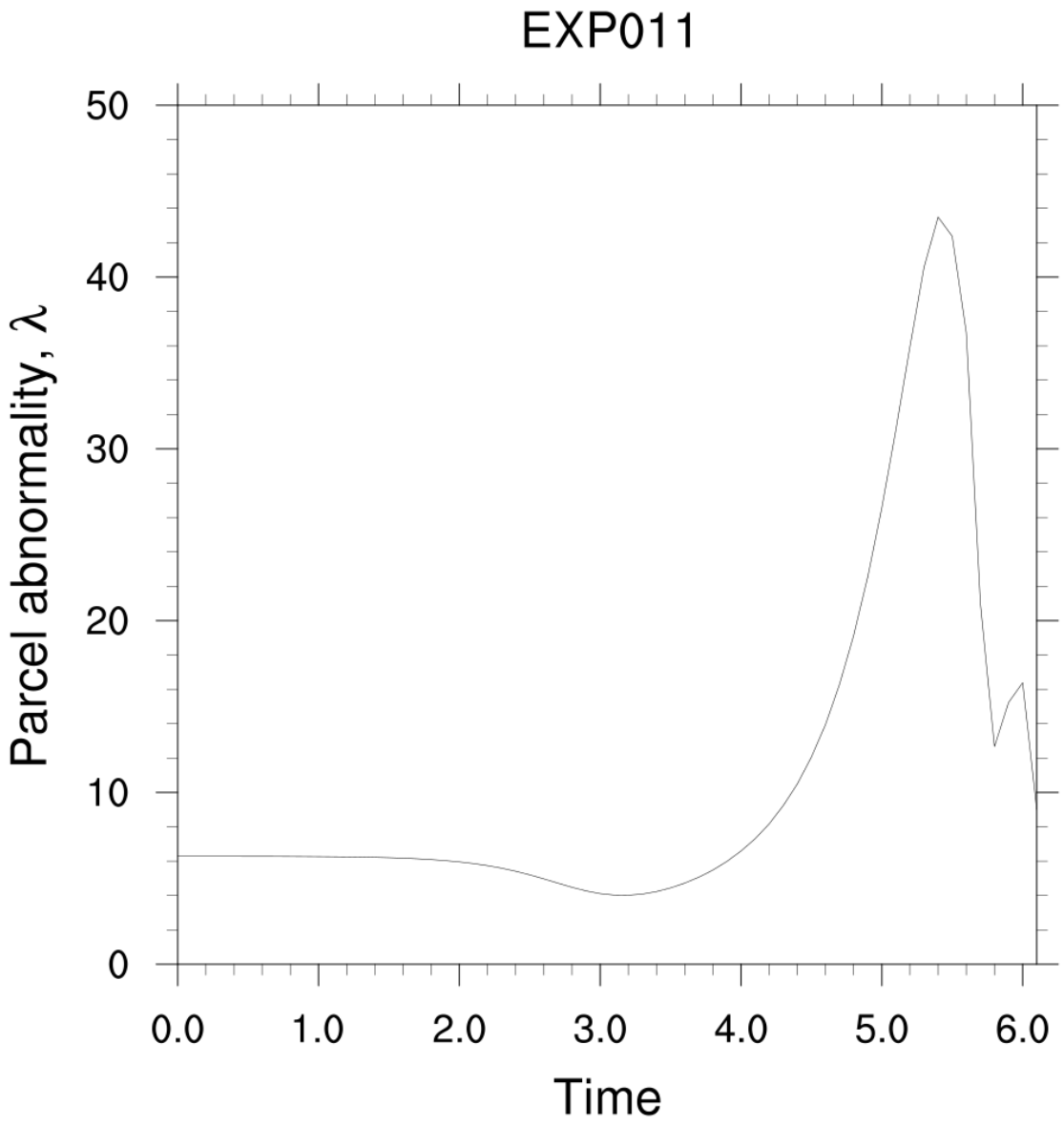

661

662 Fig. 6. Abnormality of P as a function of time.

663

664 Fig. 7 shows the evolution of parcel kinetic energy KE ≡ $q^2/2$, static energy σ, $L \equiv q^2/2 -$
665 σ, and Bernoulli function $B \equiv q^2/2 + \sigma$. These quantities change rapidly at $t = 5.4$. The
666 maximum values of KE and L, and the minimum value of σ occur at $t = 5.6$ as the parcel
667 enters the tornado. Loss of Bernoulli function occurs between $t = 5.4$ and 5.6.

668

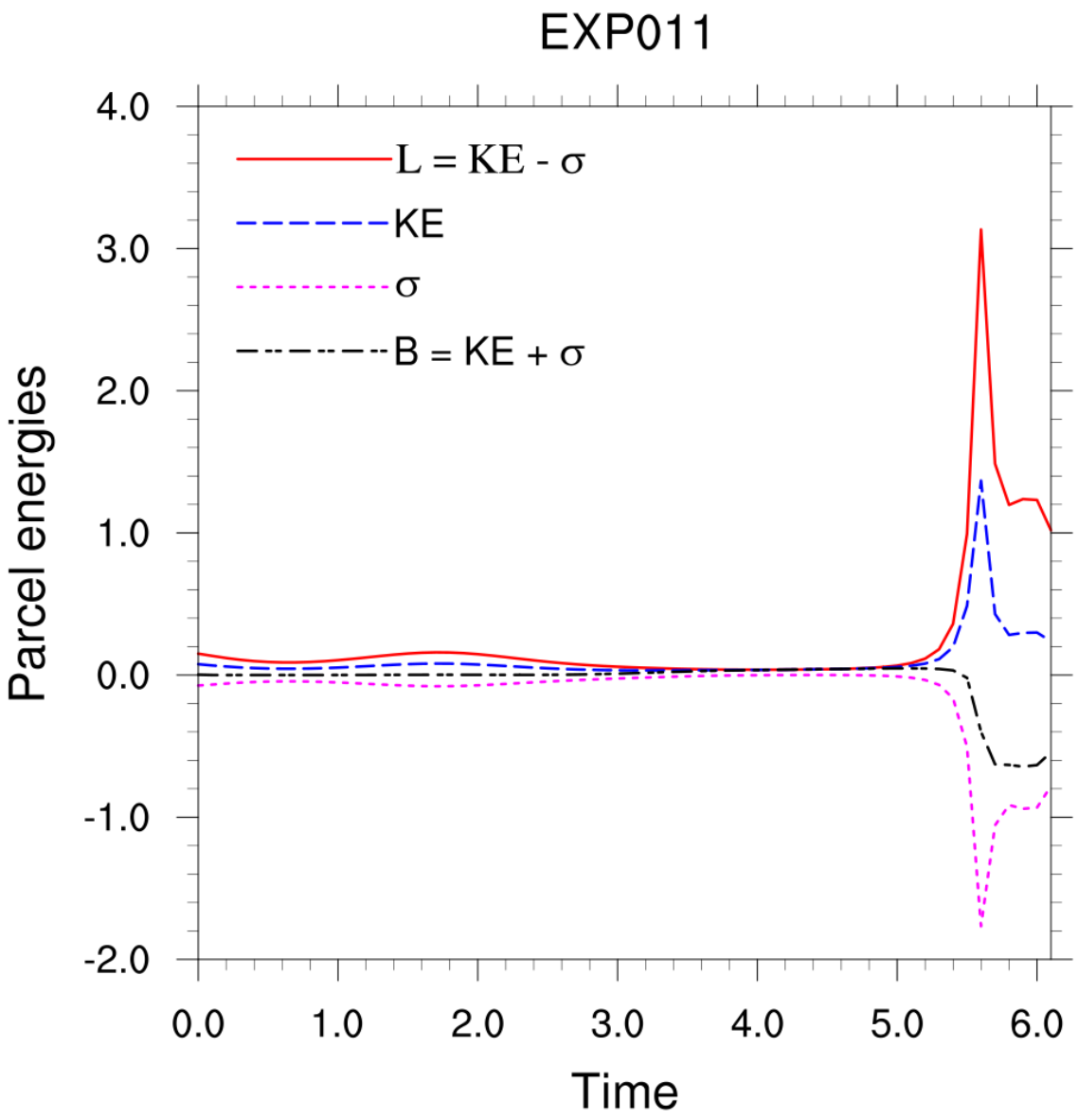

669

670 Fig. 7. Parcel energies as functions of time.

671

672 Fig. 8 shows the evolution of the parcel's kinetic energy and the accumulated kinetic
673 energy due to terms in the kinetic energy equation (2.6) as functions of time. The parcel kinetic
674 energy rises rapidly at $t = 5.4$, peaks at $t = 5.6$ due to the accumulated work done by the
675 pressure-gradient force (PGF), and declines thereafter due to adverse PGF and increased KE
676 dissipation. The accumulated work of the friction force is an energy sink and that of
677 hydrometeor drag is negligible. The computational error is again insignificant.

678

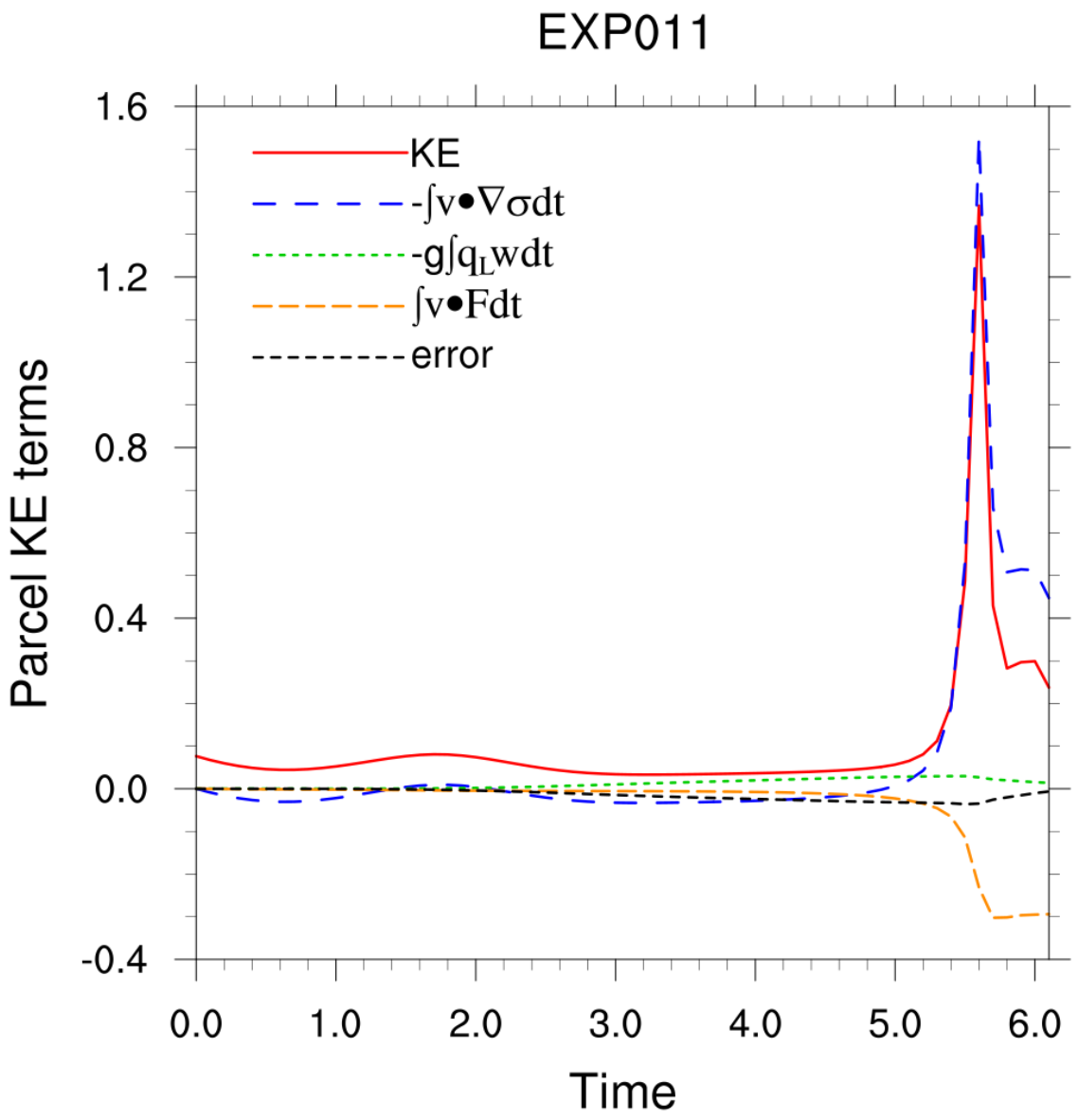

Fig. 8. Parcel kinetic energy and integrals from $t = 0$ to t of terms in (2.6) as functions of time. Each colored curve is the integral following parcel P of the term of the same color in (2.6).

6. Tornadogenesis from a control-volume perspective

Even when the flow is steady, large changes in parcel variables occur naturally as a parcel approaches the tornado. In this section, we demonstrate that local changes due to rapidly evolving flow also occur extremely swiftly. We do this by computing mean values in a surface-based cylindrical control volume (or corner region) that encloses the tornado once it forms. The radius and height of the cylinder are 0.07 and 0.1, respectively, or 845 m by 1183

m in dimensional terms. We computed the terms in (2.29), (2.30), (2.31) and (2.32) to obtain the angular-momentum, helicity kinetic-energy, and $\nabla^2 B$ budgets for the control volume. The colors of the terms in the equations correspond to the colors of the curves in Figs. 10, 11, 12 and 13.

Fig. 9 shows how rapidly the pressure and the Bernoulli function fall and the kinetic energy and Lagrangian density rise in the cylinder. The energies begin rapid changes at roughly one time unit (6 min) prior to tornado formation.

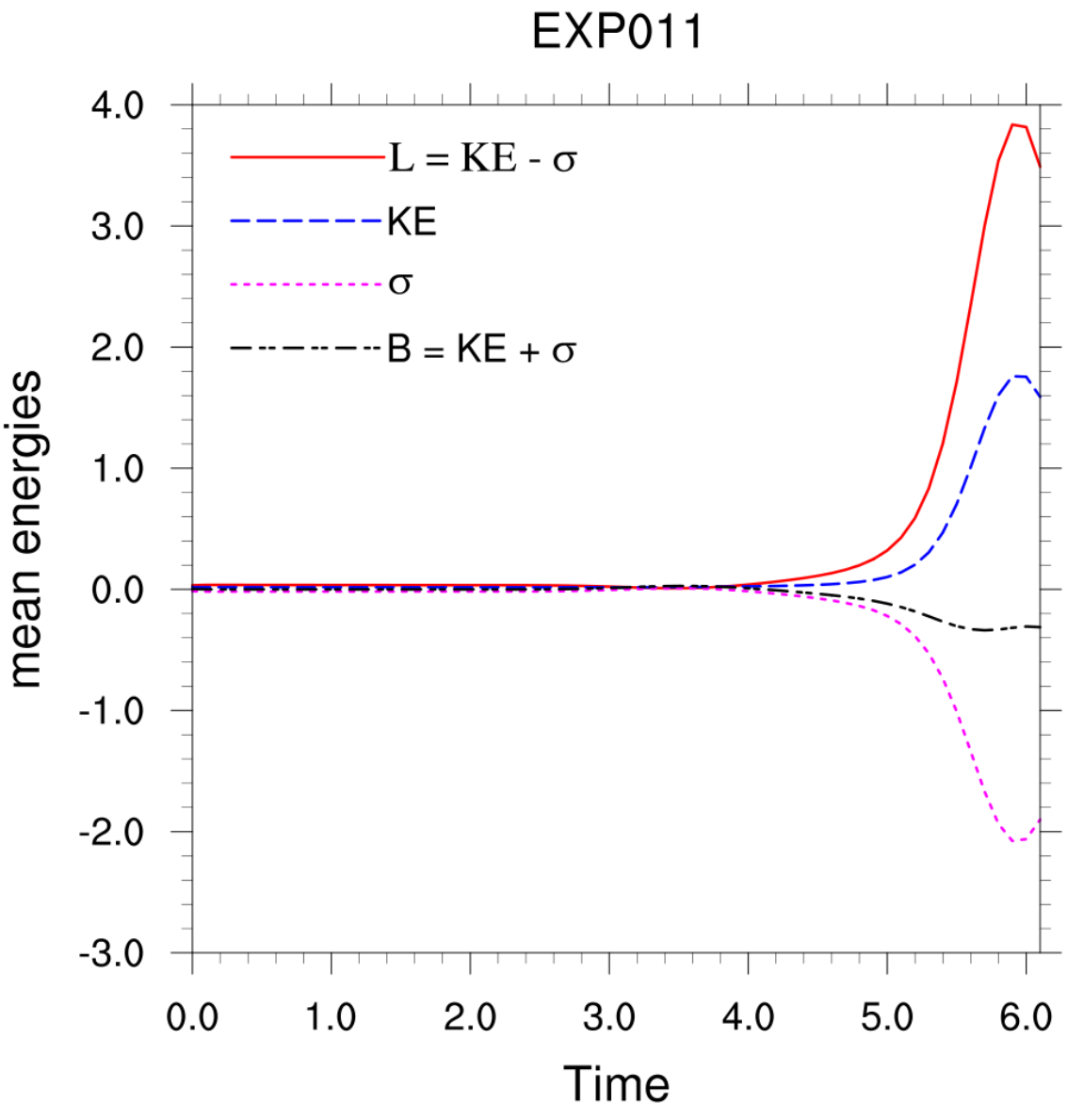

Fig. 9. Mean energies in the control volume as functions of time.

The mean AM in the cylinder starts to increase only about three minutes before the tornado forms (Fig. 10). The increase is due to the cumulative effect of AM advection into the cylinder. Minor amounts of AM are lost to time-integrated ground and outward diffusion. As gradients of AM become large, the rate of outward diffusion eventually balances the rate of inward advection. The mean AM is then at its maximum. The error or residual is trivial in this and all other control-volume budgets.

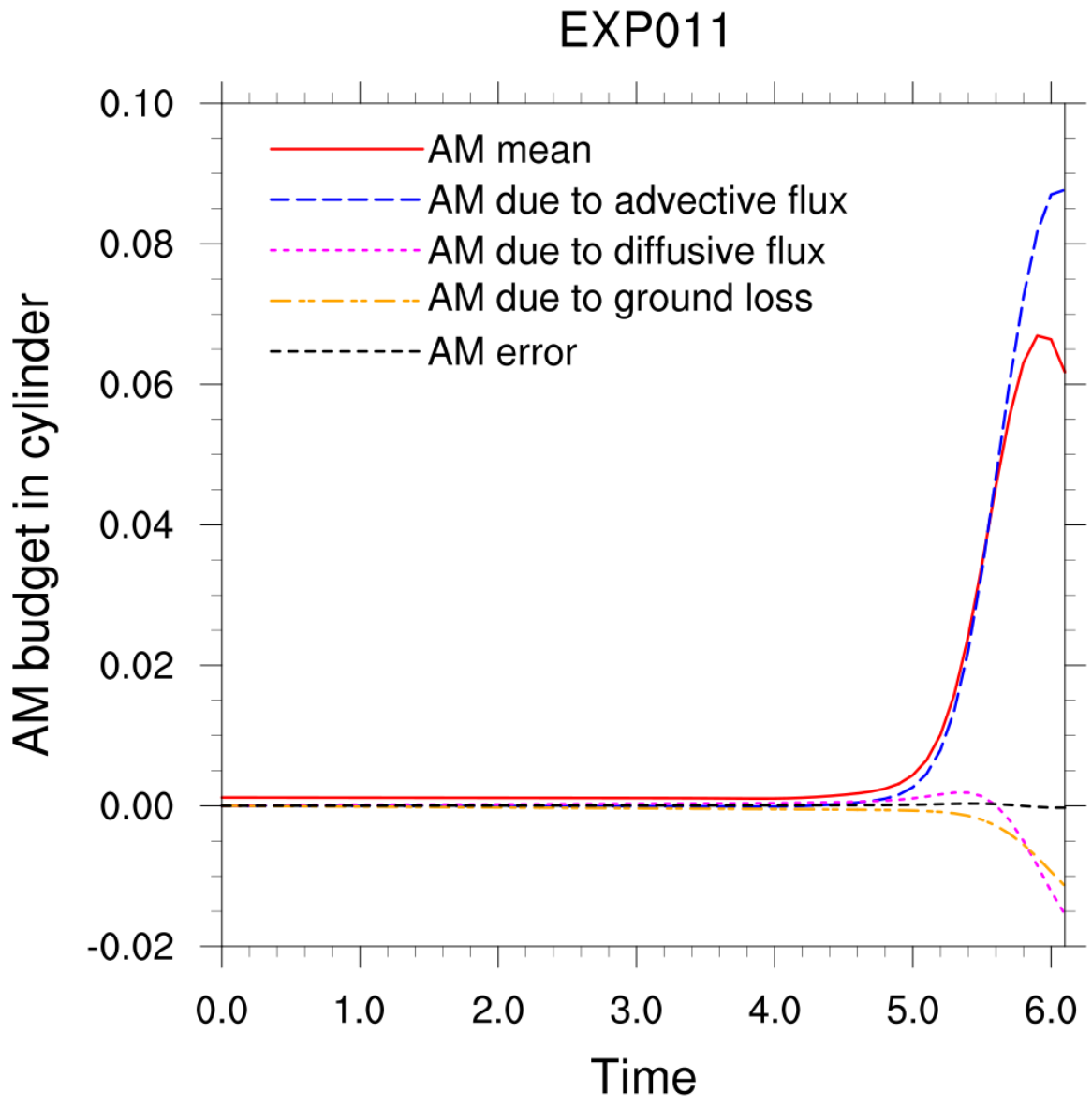

Fig. 10. Evolution of the cylinder's angular-momentum balance. The fluxes are over the closed surface of the cylinder. See (2.29) for terms.

712 Fig. 11 shows dramatic increase in the cylinder's mean helicity just prior to and during
713 the tornado. Almost all of the rapid increase in mean helicity is due to the accumulated flux
714 of $L\omega$ [the blue terms in (2.30)]. More specifically, it is due to accumulated $L\omega$ flux out of
715 the top of the cylinder (the second blue term); accumulated $L\omega$ flux at the side (the first blue
716 term) is negative (Fig. 12). Accumulated advection of helicity into the cylinder (the magenta
717 term) is small in comparison. The viscous term in (2.30) produces negative helicity and
718 ultimately curtail the tornado's helicity gain. The hydrometeor term is negligible.

719

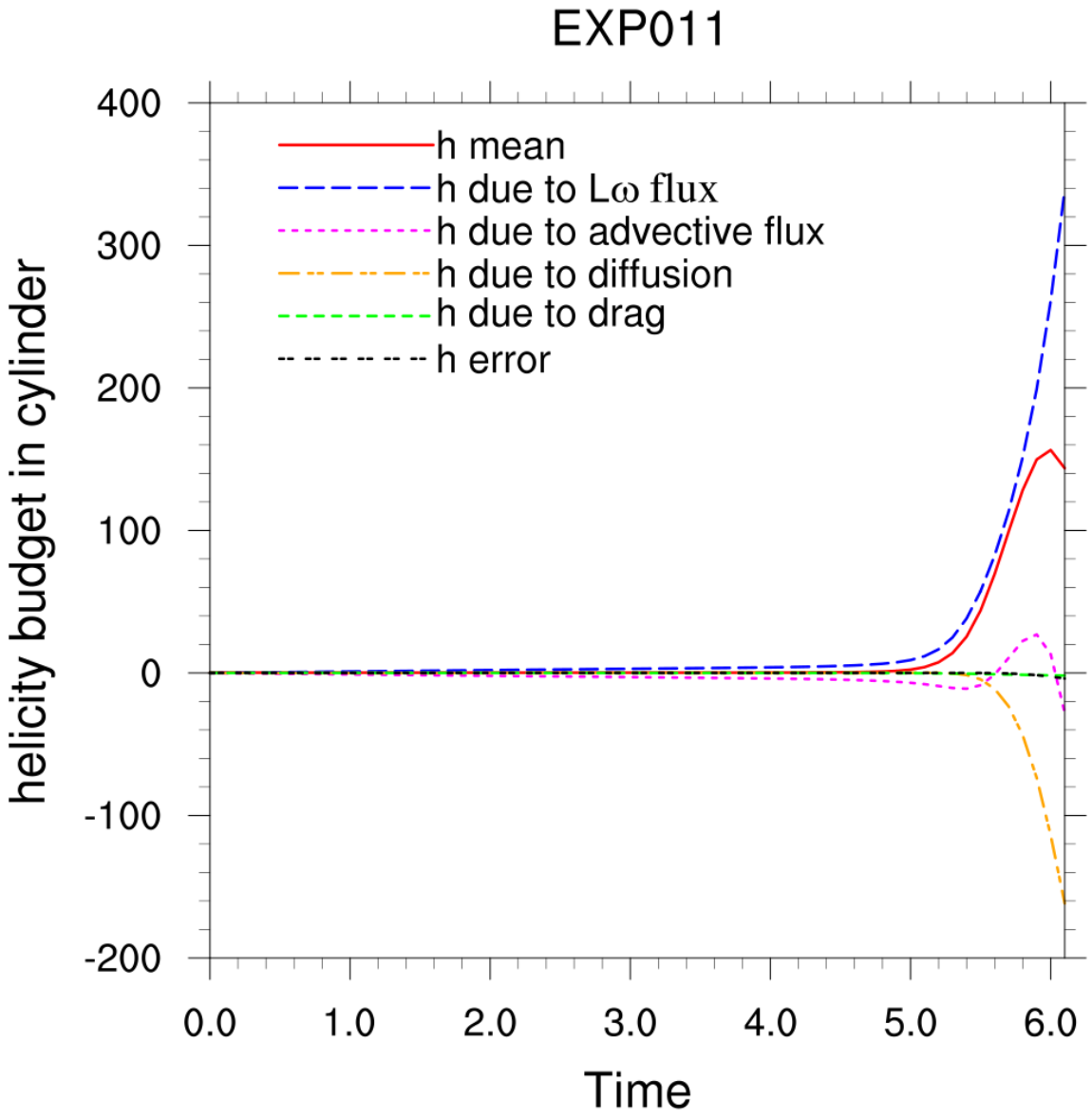

720

721 Fig. 11. The cylinder's helicity budget over time. See (2.30) for terms.

722

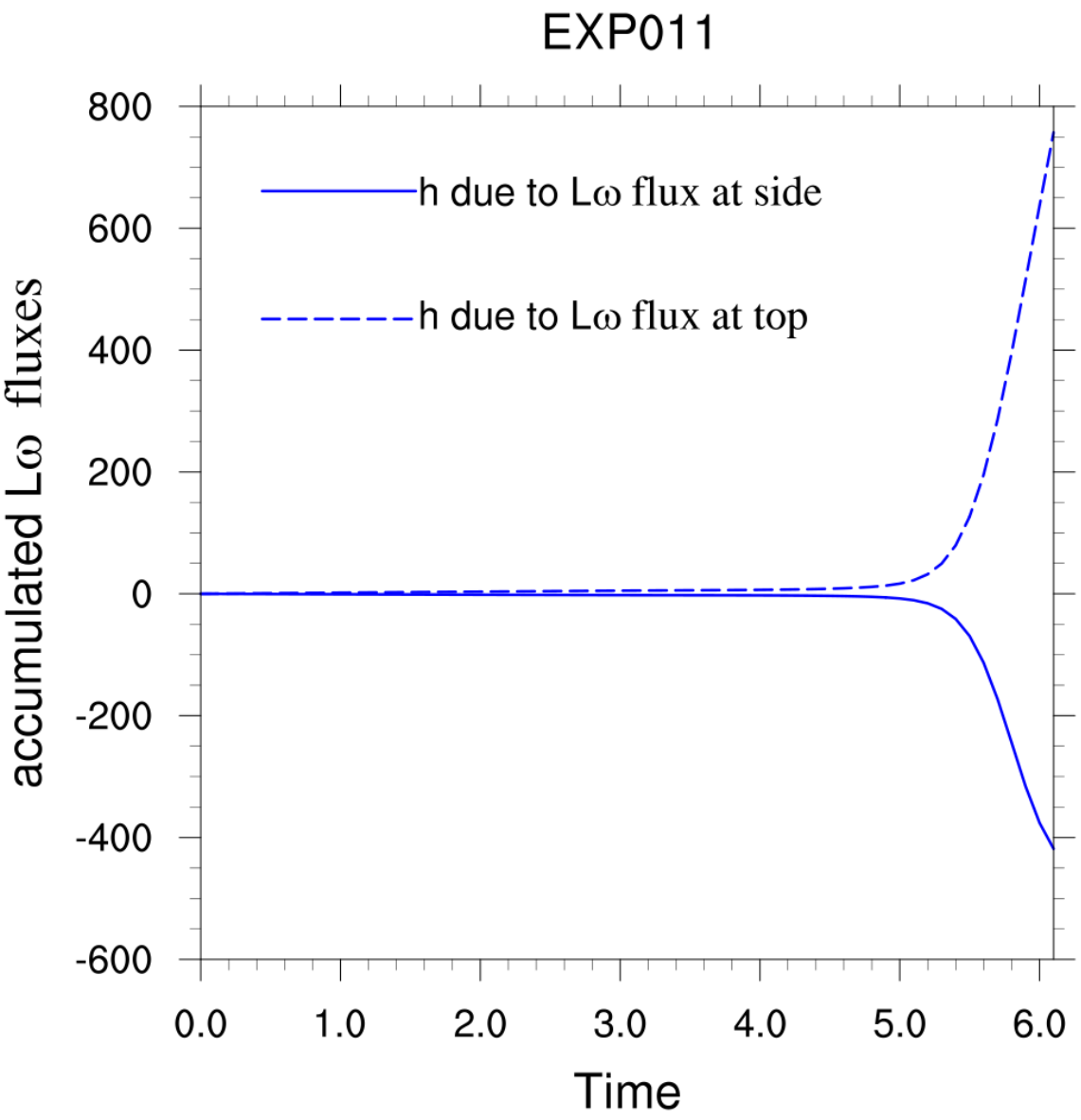

723

724 Fig. 12. The first and second blue terms in (2.30).

725

726 Fig. 13 shows how the cylinder's kinetic-energy budget evolves. The increase in mean
727 KE is due entirely to $-\mathbf{v}\bullet\nabla B$, which is the work performed by the pressure-gradient force plus
728 KE that is advected into the volume. Work by the hydrometeor-drag force is negligible.
729 Friction dissipates KE as expected. The mean KE plateaus when frictional dissipation of KE
730 instantaneously matches the KE advection and the positive work done by the PGF.

731

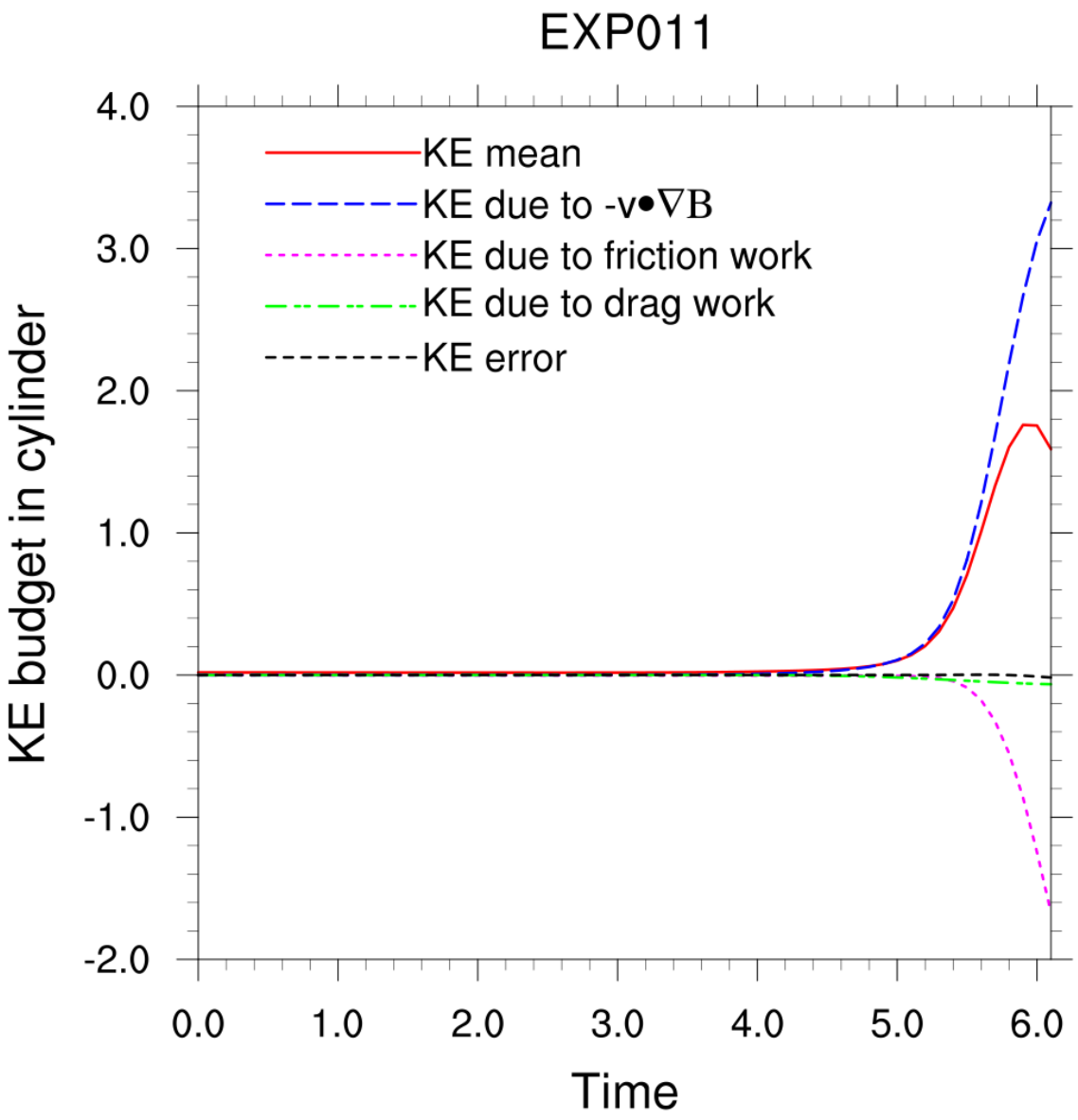

732

733 Fig. 13. Mean kinetic energy in the cylinder and the causes of its increase. See (2.31) for terms.

734

735 Fig. 14 presents the budget for the volume mean of $\nabla^2 B$, the Laplacian of Bernoulli
736 function. Export of the Lamb vector, $\mathbf{v}\times\boldsymbol{\omega}$ through the side of the cylinder accounts for most
737 of the mean $\nabla^2 B$. There is some loss of $\nabla^2 B$ from import of $\mathbf{v}\times\boldsymbol{\omega}$ through the top. Export
738 arising from the water-loading terms in (2.32) is negligible. Since $\nabla^2 B$ is correlated with $-B$
739 (c.f., Figs. 9 and 14), outward transport of Lamb vector is associated with loss of B in the
740 tornado.

741

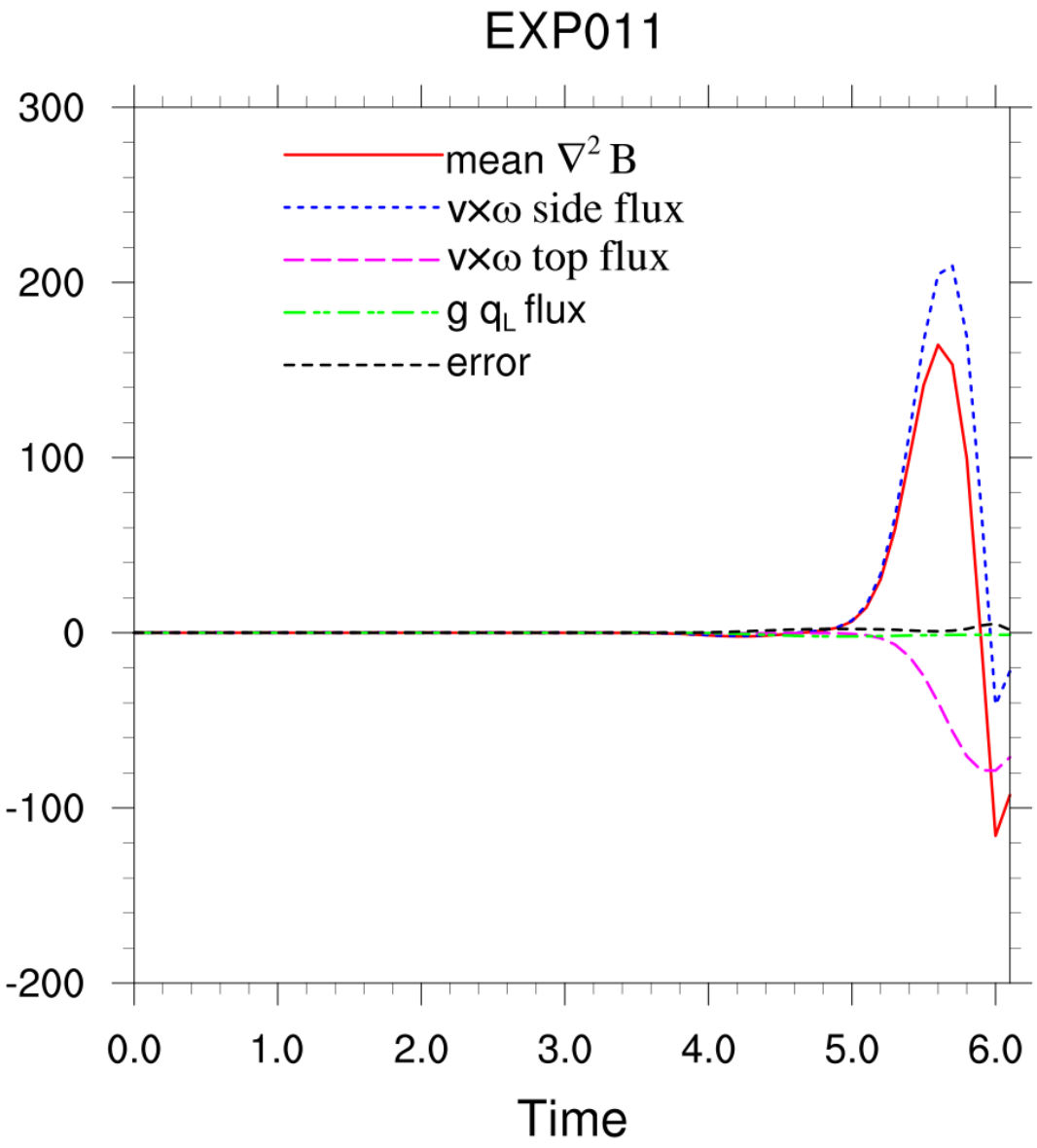

742

743 Fig. 14. The mean Laplacian of B in the cylinder and fluxes out of the cylinder versus time. See (2.32)
744 for terms.

745

746 Fig. 15 compares the mean magnitudes in the cylinder of the helicity and Lamb vector.
747 During the tornado, the helicity is an order of magnitude larger than the Lamb vector. Hence,
748 the vorticity in the tornado is predominantly streamwise. Nevertheless, the Lamb vector is
749 still important because, without it, the vertical vorticity of parcels would not turn weakly
750 cyclonic shortly before entering the updraft (Davies-Jones 2025c), AM would not be
751 advected into the near-ground updraft, and there would be no loss of Bernoulli function in the
752 vortex.

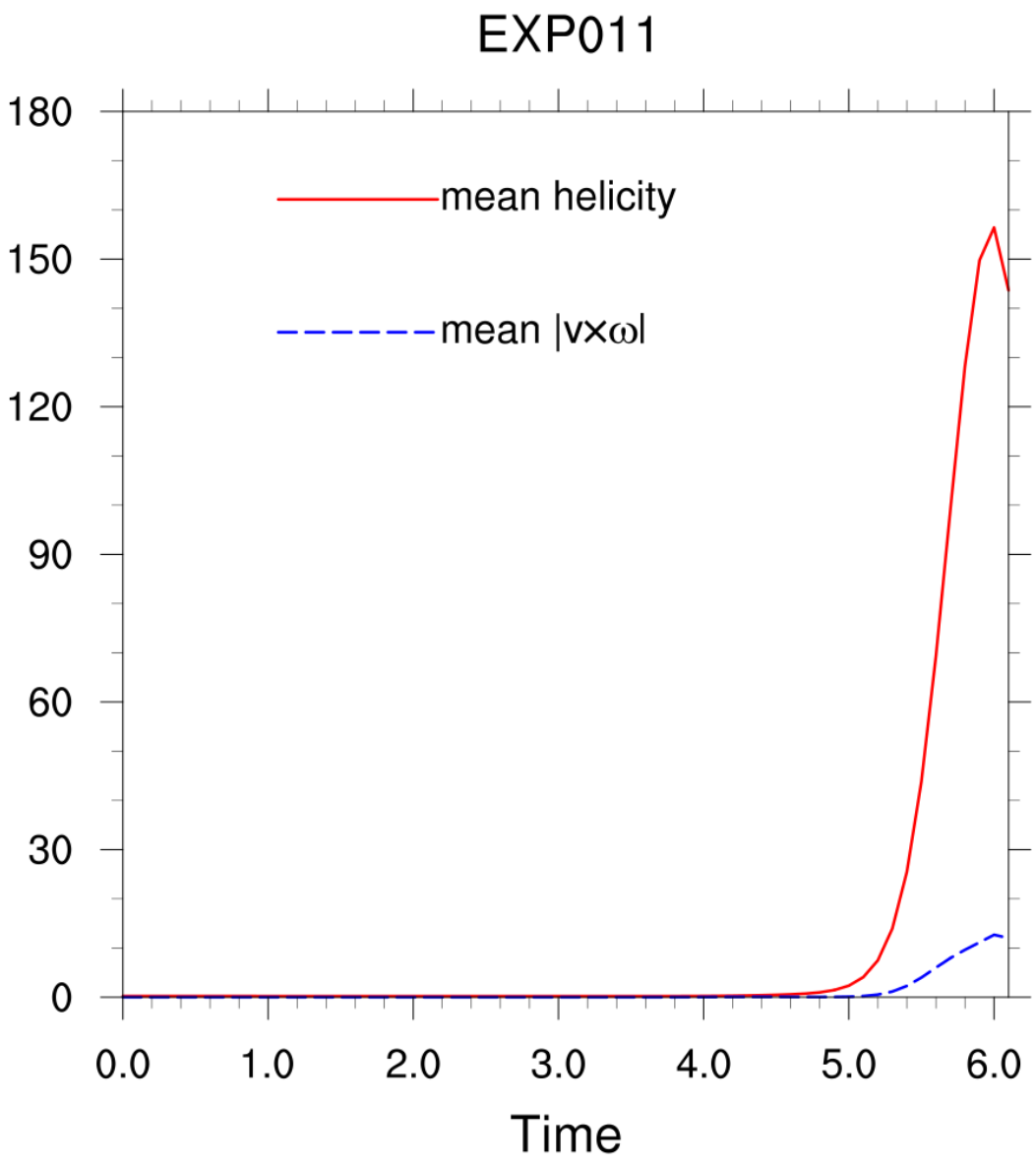

Fig. 15. Evolution of mean helicity and mean magnitude of Lamb vector in cylinder.

Over the course of the simulation, the mean convergence and vertical vorticity in the cylinder increase by factors of 15 and 38, respectively (Fig. 16). These variables start increasing rapidly about three minutes before tornado formation, indicating intensive tilting and stretching of vortex tubes. Amplification of convergence coincides with the contraction of the low-level updraft. Estimates of the time it takes for a tornado to form usually assume a constant larger-scale convergence (Davies-Jones, 1986, 2015). The formation time reduces

763 greatly when the local convergence increases by an order of magnitude during
764 tornadogenesis.

765

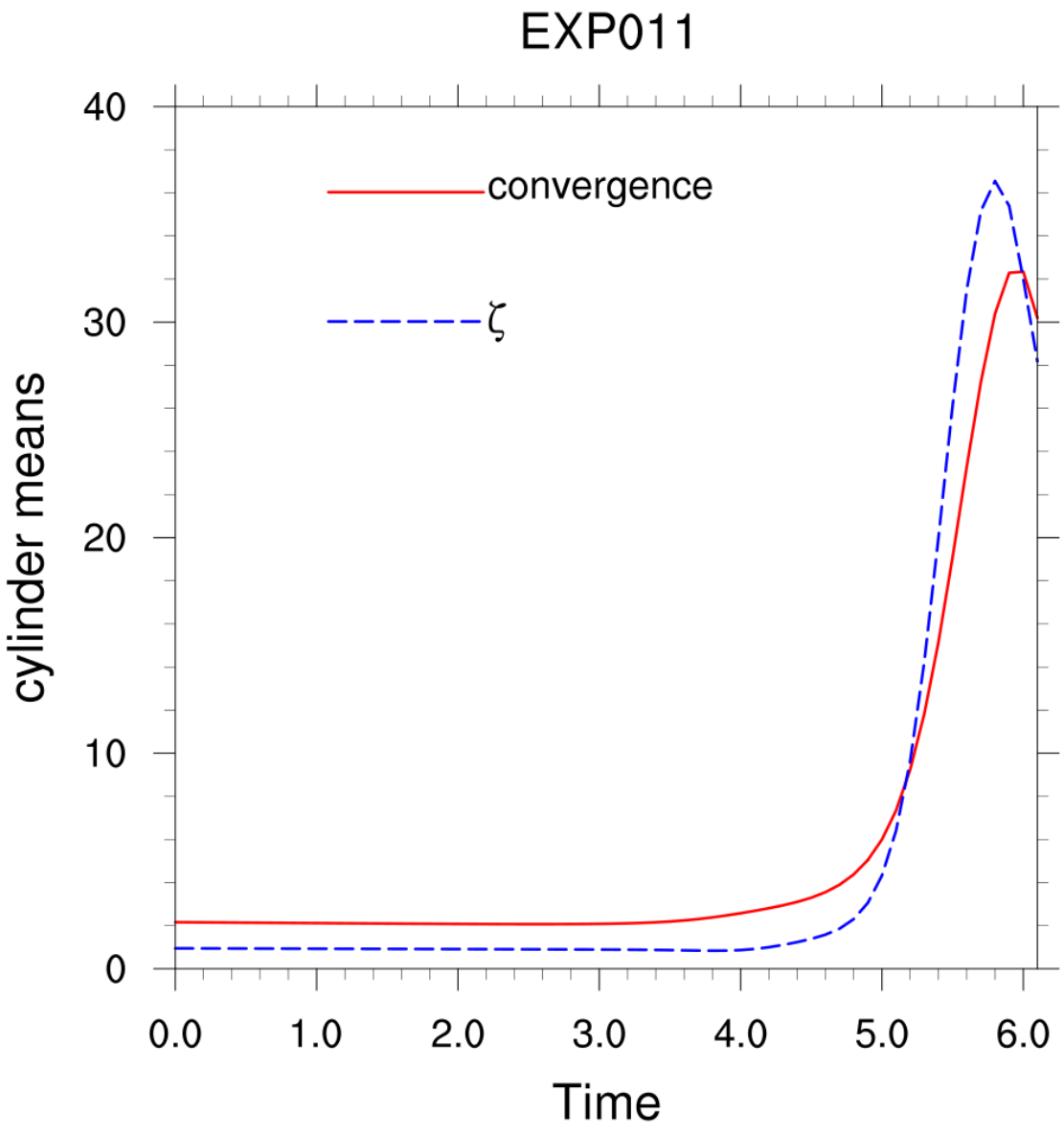

766

767 Fig. 16. Evolution of mean convergence and mean vertical vorticity in cylinder.

768

769 **7. Discussion**

770 The simulation demonstrates that a tornado can form very rapidly from the collapse of a
771 midlevel mesocyclone. Initially, there is very little weather occurring in the cylindrical
772 corner region of the domain discussed in section 6. Although there is a rotating updraft

773 overhead, most of the inflow rises in broad ascent in response to low static energy on the
774 updraft's axis at its mid-height and surface winds are weak. For a tornado to form, the
775 volume flow rate, and the AM, helicity and kinetic energy in the cylinder must increase
776 greatly.

777 When rain falls from high in the storm and initiates a rainy downdraft near the updraft
778 edge, the flow changes gradually at first and then extremely rapidly. The rainy downdraft
779 and its outflow advect AM downward and inward towards the axis. AM in the cylinder
780 increases owing to AM advection through its side. In response to the increase in near-ground
781 windspeed, the minimum in static energy moves downward. Work by the pressure-gradient
782 force amplifies KE in the cylinder. Helicity density in the cylinder increases greatly due to
783 flux of $L\omega$ though its side. The simulated tornado forms very quickly due to intense tilting
784 and stretching of barotropic vorticity as the tornado-scale convergence increases by more
785 than an order of magnitude.

786 As noted by Rotunno and Bluestein (1984), most diagnoses of the origins of low-level
787 rotation in supercells discuss the variation of vorticity along parcel trajectories or the
788 circulation around material circuits without discussion of the forces required to bring parcels
789 to close proximity of the circulation center. Surprisingly, a parcel P that enters the tornado in
790 the current simulation does not descend in the rainy downdraft. Instead, it comes at low
791 heights from larger radii just before outflow from the rainy downdraft blocks this route. It
792 keeps low to the ground because it is accelerated by a pressure-gradient force that is now
793 predominantly inward and only slightly upward (animation D). In the initial Beltram state,
794 the pressure-gradient force in the updraft at low heights is upward and outward so the ascent
795 is broad. The helicity of P increases by a factor of 100 between the initial time and time of
796 entry into the tornado.

797 Tornado formation in supercell storms is usually divided into three distinct stages, namely
798 genesis of a rotating updraft aloft, development of rotation near the ground, and spin up of the
799 near-ground rotation into a tornado that exceeds the thermodynamic speed limit (Davies-
800 Jones 2015). We will now examine how the axisymmetric model follows this progression.

801 The updraft rotates aloft simply as a result of upward tilting of storm-relative
802 environmental streamwise vorticity. This was demonstrated via linear theory by DJ84 and
803 Davies-Jones and Markowski (2021, p. 2899), and with nonlinear effects by Davies-Jones
804 (2022, p. 1265). Because the environment is asymmetric, an axisymmetric model cannot

replicate this process. Instead, it assumes stage 1 has established a rotating updraft, which is included in its Beltrami initial state, and starts with stage 2, when the initial state is unbalanced by the introduction of hydrometeors.

The latest conceptual tornadogenesis model (Fischer et al. 2024) does not consider a symmetric vortex until the end of stage 2 whereas the DJ08 model is naturally axisymmetric throughout stages 2 and 3. In the axisymmetric simulation, near-ground rotation results from downward and inward advection of angular momentum, or, equivalently, from the azimuthal component of the Lamb vector. These processes are consequences of the hydrometeor drag force causing the streamlines to separate from the vortex lines in the downdraft. In the Fischer et al. conceptual model, negative buoyancy forces (which are excluded from the DJ08 model by design) achieve the same effect.

Acknowledgments. Thanks to Brian Davies-Jones for installing NCAR Command Language on my computer and helping me with the website. In memory of Steven D-J.

Data Availability Statement. No datasets were generated or analyzed during the present study.

REFERENCES

Adlerman, E. J., K. K. Droegemeier, and R. Davies-Jones, 1999: A numerical simulation of cyclic mesocyclogenesis. *J. Atmos. Sci.,* **56,** 2045-2069.

Adrian, R. J., 1982: Comment on "A Note on Poisson's Equation for Pressure in a Turbulent Flow". *Phys. Fluids*, **25**, 577.

Barnes. S. L., 1970: Some aspects of a severe, right-moving thunderstorm deduced from mesonet rawinsonde observations. *J Atmos. Sci*., **27**, 634-648.

Batchelor, G. K., 1967: *An Introduction to Fluid Dynamics*. Cambridge University Press, 615 pp.

Bradshaw, P., and Y. M. Koh, 1981: A Note on Poisson's Equation for Pressure in a Turbulent Flow. *Phys. Fluids*, **24**, 777.

834 Davies-Jones, R. P., 1984: Streamwise vorticity: The origin of updraft rotation in supercell
835 storms. *J Atmos. Sci*., **41**, 2991-3006.

836 Davies-Jones, R. P., 1986: Tornado dynamics. *Thunderstorm Morphology and Dynamics,*
837 2nd ed., E. Kessler, Ed., University of Oklahoma Press, 197–236.

838 Davies-Jones, R. P., 2002: Linear and nonlinear propagation of supercell storms. *J. Atmos.*
839 *Sci.,* **59,** 3178–3205.

840 Davies-Jones, R. P., 2008: Can a descending rain curtain in a supercell instigate
841 tornadogenesis barotropically? *J Atmos. Sci*., **65**, 2469-2497.

842 Davies-Jones, R. P., 2015: A review of supercell and tornado dynamics. *Atmos. Res*., **158**–
843 **159**, 274–291.

844 Davies-Jones, R. P., 2022: Theory of parcel vorticity evolution in supercell-like flows. *J.*
845 *Atmos. Sci.*, **79**, 1253-1270.

846 Davies-Jones, R. P., 2025a: Theory of parcel helicity in supercell-like flows. *D-J Retirement*
847 *Papers*, **1**.

848 Davies-Jones, R. P., 2025b: Parcel helicity in a secondary-flow model. *D-J Retirement*
849 *Papers*, **2**.

850 Davies-Jones, R. P., 2025c: On the development of near-ground rotation during
851 tornadogenesis. *D-J Retirement Papers*, **4**.

852 Davies-Jones, R. P., and H. E. Brooks, 1993: Mesocyclogenesis from a theoretical
853 perspective. *The Tornado: Its Structure, Dynamics, Prediction, and Hazards, Geophys.*
854 *Monogr.*, No. **79**, Amer. Geophys. Union, 105–114.

855 Davies-Jones, R. P., and P. M. Markowski, 2021: Circulation around a constrained curve: An
856 alternative analysis tool for diagnosing the origins of tornado rotation in numerical
857 supercell simulations. *J. Atmos. Sci*.,**78**, 2895-2909.

858 Davies-Jones, R. P., D. W. Burgess, and L. R. Lemon, 1976: An atypical tornado-producing
859 cumulonimbus. *Weather*, **31**, 337-347.

860 Davies-Jones, R. P., D. W. Burgess, L. R. Lemon, and D. Purcell 1978: Interpretation of
861 Surface Marks and Debris Patterns from the 24 May 1973 Union City, Oklahoma
862 Tornado. *Mon. Wea. Rev*., **106**, 12-21.

863 Davies-Jones, R. P., R. J. Trapp, and H. B. Bluestein, 2001: Tornadoes and tornadic storms.
864 *Meteor. Monogr.*, No. 50, 167–221.

865 Dutton, J. A., 1976: *The Ceaseless Wind*. McGraw-Hill, 579 pp.

866 Fiedler, B. H., 1994: The thermodynamic speed limit and its violation in axisymmetric
867 numerical simulations of tornado-like vortices. *Atmosphere-Ocean*, **32**, 335-359.

868 Fiedler, B. H., and R. Rotunno, 1986: A theory for the maximum windspeeds in tornado-like
869 vortices. *J. Atmos. Sci.*, **43**, 2328-2340.

870 Fujita, T. T., 1973; Proposed mechanism of tornado formation from rotating thunderstorm.
871 Preprints, *Eighth Conf. on Severe Local Storms,* Denver, CO, Amer. Meteor. Soc., 191–
872 196.

873 Fujita, T. T., 1975; New evidence from April 3–4, 1974 tornadoes. Preprints, *Ninth Conf. on*
874 *Severe Local Storms*, Norman, OK, Amer. Meteor. Soc., 248–255.

875 Haltiner, G. J., and F. L. Martin, 1957: *Dynamical and Physical Meteorology*. McGraw-Hill,
876 470 pp.

877 Hildebrand, F. B., 1962: Advanced Calculus for Applications. Prentice-Hall, 646 pp.

878 Lewellen, D. C., and W. S. Lewellen, 2007a: Near-surface intensification of tornado vortices.
879 *J. Atmos. Sci.,* **64,** 2176–2194.

880 Lewellen, D. C., and W. S. Lewellen, 2007b: Near-surface vortex intensification through
881 corner flow collapse. *J. Atmos. Sci.,* **64,** 2195–2209.

882 Lewellen, D. C., W. S. Lewellen, and J. Xia, 2000: The influence of a local swirl ratio on
883 tornado intensification near the surface. *J. Atmos. Sci.,* **57,** 527–544.

884 Lilly, D. K., 1986: The structure, energetics and propagation of rotating convective storms.
885 Part II: Helicity and storm stabilization. *J Atmos. Sci*., **43**, 126-140.

886 Margenau, H., and G. M. Murphy, 1956: *The Mathematics of Physics and Chemistry*. 2nd ed.
887 Van Nostrand, 604 pp.

888 Rotunno, R., and H. B. Bluestein, 2024: Recent developments in tornado theory and
889 observations. *Rep. Progr. Phys*., **87**, 114801.

890 Rotunno, R., and J. B. Klemp, 1985: On the rotation and propagation of simulated supercell
891 thunderstorms. *J. Atmos. Sci.*, **42**, 271–292.

892 Rotunno, R., P. M. Markowski, and G. H. Bryan, 2017: “Near ground” vertical vorticity in
893 supercell thunderstorm models. *J. Atmos. Sci.*, **74**, 1757-1766.

894 Scorer, R. S., 1997: *Dynamics of Meteorology and Climate*. Praxis, 686 pp.

895 Shapiro, A. H., 1972: Vorticity. *Illustrated Experiments in Fluid Mechanics: The NCFMF*
896 *Book of Film Notes*. MIT Press, 63-74. Available online at
897 http://web.mit.edu/hml/ncfmf/09VOR.pdf

898 Shapiro, A., 1993: The use of an exact solution of the Navier–Stokes equations in a validation
899 test of a three-dimensional nonhydrostatic numerical model. *Mon. Wea. Rev*., **121**, 2420–
900 2425.

901 Siebert, P., 1993: Convergence and accuracy of numerical methods for trajectory
902 calculations. *J. Appl. Meteor*., **32**, 558-566.

903 Vande Guchte, A., and J. M. L. Dahl 2018: Sensitivities of parcel trajectories beneath the
904 lowest scalar model level of a Lorenz vertical grid. *Mon. Wea. Rev*., **146**, 1427-1435.

905 Wang, A., Y. Pan, and P. M. Markowski, 2020: The influence of turbulence memory on
906 idealized tornado simulations. *Mon. Wea. Rev*., **148**, 4875-4892.

907 Wicker, L. J., and R. B. Wilhelmson, 1995: Simulation and analysis of tornado development
908 and decay within a three-dimensional supercell thunderstorm. *J. Atmos. Sci.*, **52**, 2675-
909 2703.